TU Delft

Delft University of Technology

Shallow Convective Heating in Weak Temperature Gradient Balance Explains Mesoscale Vertical Motions in the Trades

Janssens, M.; George, G.; Schulz, H.; Couvreux, Fleur; Bouniol, Dominique

DOI
10.1029/2024JD041417

Publication date
2024

Document Version
Final published version

Published in
Journal of Geophysical Research: Atmospheres

Citation (APA)
Janssens, M., George, G., Schulz, H., Couvreux, F., & Bouniol, D. (2024). Shallow Convective Heating in Weak Temperature Gradient Balance Explains Mesoscale Vertical Motions in the Trades. *Journal of Geophysical Research: Atmospheres*, *129*(18), Article e2024JD041417. https://doi.org/10.1029/2024JD041417

Important note
To cite this publication, please use the final published version (if applicable).
Please check the document version above.

Copyright
Other than for strictly personal use, it is not permitted to download, forward or distribute the text or part of it, without the consent of the author(s) and/or copyright holder(s), unless the work is under an open content license such as Creative Commons.

Takedown policy
Please contact us and provide details if you believe this document breaches copyrights.
We will remove access to the work immediately and investigate your claim.

This work is downloaded from Delft University of Technology.
For technical reasons the number of authors shown on this cover page is limited to a maximum of 10.

Check for updates

JGR Atmospheres

RESEARCH ARTICLE
10.1029/2024JD041417

Shallow Convective Heating in Weak Temperature Gradient Balance Explains Mesoscale Vertical Motions in the Trades

M. Janssens[1,2], G. George[2,3], H. Schulz[4,5], Fleur Couvreux[6], and Dominique Bouniol[6]

[1]Wageningen University & Research, Wageningen, The Netherlands, [2]Delft University of Technology, Delft, The Netherlands, [3]Max Planck Institute for Meteorology, Hamburg, Germany, [4]Cooperative Institute for Climate, Ocean & Ecosystem Studies (CICOES), Seattle, WA, USA, [5]University of Washington, Seattle, WA, USA, [6]CNRM, Université de Toulouse, Météo-France, CNRS, Toulouse, France

Key Points:

- A realistic large-eddy simulation adequately represents vertical motion in shallow mesoscale circulations recently observed in the trades
- At mesoscales, shallow convective heating causes the vertical motion, inverting the classical view that circulations control shallow clouds
- Water vapor convergence with the circulations is likely key to develop the mesoscale shallow convection patterns

Supporting Information:

Supporting Information may be found in the online version of this article.

Correspondence to:

M. Janssens,
martin.janssens@wur.nl

Citation:

Janssens, M., George, G., Schulz, H., Couvreux, F., & Bouniol, D. (2024). Shallow convective heating in weak temperature gradient balance explains mesoscale vertical motions in the trades. *Journal of Geophysical Research: Atmospheres*, *129*, e2024JD041417. https://doi.org/10.1029/2024JD041417

Received 22 APR 2024
Accepted 3 SEP 2024

Abstract Earth's climate sensitivity depends on how shallow clouds in the trades respond to changes in the large-scale tropical circulation with warming. In canonical theory for this cloud-circulation coupling, it is assumed that the clouds are controlled by the field of vertical motion on horizontal scales larger than the convection's depth (∼1 km). This assumption has been challenged both by recent in situ observations, and idealized large-eddy simulations (LESs). Here, we therefore bring together the recent observations, new analysis from satellite data, and a 40-day, large-domain (1600 × 900 km^2) LES of the North Atlantic from the 2020 EUREC^{4}A field campaign, to study the interaction between shallow convection and vertical motions on scales between 10 and 1,000 km (mesoscales), in settings that are as realistic as possible. Across all data sets, the shallow mesoscale vertical motions are consistently represented, ubiquitous, frequently organized into circulations, and formed without imprinting themselves on the mesoscale buoyancy field. Therefore, we use the weak-temperature gradient approximation to show that between at least 12.5–400 km scales, the vertical motion balances heating fluctuations in groups of precipitating shallow cumuli. That is, across the mesoscales, shallow convection controls the vertical motion in the trades, and does not simply adjust to it. In turn, the mesoscale convective heating patterns appear to consistently grow through moisture-convection feedback. Therefore, to represent and understand the cloud-circulation coupling of trade cumuli, the full range of scales between the synoptics and the hectometer must be included in our conceptual and numerical models.

Plain Language Summary The tropical oceans are covered by shallow cumulus clouds, partially controlled by a gentle downward vertical motion associated with large (larger than 1,000 km) tropical circulations. Changes in these circulations, for example due to warming climate, can therefore change the shallow cloudiness, and their climatological cooling. Hence, understanding this cloud-circulation coupling is an important challenge. Here, we study the cloud-circulation coupling over areas of tens to hundreds of kilometres ("mesoscales") in simulations, field observations and satellite data of unprecedented detail. We find that in mesocale domains, circulations do not just control shallow clouds, as historically thought. Instead, the heating in clusters of rainy cumuli drives the circulations, as suggested by recent idealized simulations. The question is then: what controls these mesoscale cloud patterns? In the detailed simulations, they develop in unusually moist layers, which are further moistened by the circulations. Since moister layers support more clouds, the clouds and circulations grow together. Hence, our results show that on top of the classical sketch of clouds responding to large circulations, lies a dynamic mesoscale picture of two-way interactions between the two, which we must understand if we wish to predict the distribution of clouds over the tropical oceans in our transient climate.

1. Introduction

In marine trade-wind regimes, a layer of shallow convection usually covers the atmosphere's lower 1–3 km. In all conceptual models for such cumulus-topped boundary layers, the vertical motion on the O (1,000 km) scale of a trade-wind region is an important control on the convection: Given fixed, imposed radiative cooling and horizontal cold-air advection to destabilize the column, variations in the advective heating and drying with the large-scale descent control variations in the depth and coverage of the clouds in the trades (e.g., Albrecht et al., 1979; Betts, 1973; Betts & Ridgway, 1989; Neggers et al., 2006). This view is taken, for example, in (a) most large-eddy simulation (LES) studies of trade-cumuli (e.g., Blossey et al., 2013; Jansson et al., 2023; Siebesma et al., 2003; Stevens et al., 2001), which prescribe a fixed large-scale descent at the 10–100 km domain scale, (b) in shallow cloud-controlling factor (CCF) analyses, which assume that co-variability between vertical motion and cloudiness

© 2024. The Author(s).
This is an open access article under the terms of the Creative Commons Attribution-NonCommercial-NoDerivs License, which permits use and distribution in any medium, provided the original work is properly cited, the use is non-commercial and no modifications or adaptations are made.

21698996, 2024, 18, Downloaded from https://agupubs.onlinelibrary.wiley.com/doi/10.1029/2024JD041417 by Technical University Delft, Wiley Online Library on [02/10/2024]. See the Terms and Conditions (https://onlinelibrary.wiley.com/terms-and-conditions) on Wiley Online Library for rules of use; OA articles are governed by the applicable Creative Commons License

depicts the clouds adjusting to the vertical motion over O (100 km) spatial scales (S. A. Klein et al., 2017; Myers & Norris, 2013; Scott et al., 2020), and (c) in the parameterizations that represent shallow cumuli in weather and climate models (e.g., Golaz et al., 2002; Hourdin et al., 2019; Walters et al., 2019).

The conceptual sketch of O (1 km) scale shallow convection responding to O (1,000 km) scale vertical motion has served us well. Yet spatial variability in trade-wind cloudiness is usually much larger than 1 km (Denby, 2020; Janssens et al., 2021; Nuijens et al., 2014; Schulz, 2022; Stevens et al., 2020; Wood & Field, 2011), and vertical motion at scales much smaller than 1,000 km is often many times larger than needed to balance the climatological radiative cooling (Bony & Stevens, 2019; George, Stevens, Bony, Pincus, et al., 2021; Schulz & Stevens, 2018; Stephan & Mariaccia, 2021). In observations taken during the 2020 EUREC^{4}A field campaign (Bony et al., 2017; Stevens et al., 2021), this vertical motion is typically organized into O (100 km)-scale Shallow Mesoscale Overturning Circulations (SMOCs, George et al., 2023), which couple tightly to the convective mass flux and cloud-base area fraction (Vogel et al., 2022). That is, in "mesoscale" domains of O (10–1,000 km), there is a strong coupling between shallow convection and shallow circulations, which cannot be explained by O (1,000 km) scale tropical circulations controlling O (1 km) scale convection patterns. To explain how cloudy it is in such mesoscale domains, we must understand both the processes that control the large-scale vertical motion, and those that control the mesoscale variability around it.

Here, we therefore examine what determines the low-level, mesoscale vertical motion field. A clue is offered by idealized LESs on 100 km domains (Bretherton & Blossey, 2017; Janssens et al., 2023). In these simulations, condensational heating anomalies in clusters of shallow cumulus clouds would not lead to mesoscale buoyancy storage, but instead to mesoscale ascent. That is, they satisfy a form of the weak-temperature gradient (WTG) approximation (e.g., R. Klein, 2010; Sobel et al., 2001; Raymond et al., 2015), which is commonly used to explain how heating in deep convection translates to circulations across the tropics (e.g., Adames, 2022; Ahmed et al., 2021; Chikira, 2014; Held & Hoskins, 1985; Wolding et al., 2016). In this view, mesoscale patterns in trade cumuli are not merely a response to circulations; they directly drive them. However, beyond these idealized LESs, we are not aware of dedicated studies that assess the validity of WTG in the trade-wind boundary layer, or use it to link convection and circulations across the mesoscales. Therefore, our primary objective will be to validate the idealized theories in realistic settings.

We will use EUREC^{4}A and satellite observations, and the realistically forced, large-domain LESs presented by Schulz and Stevens (2023) (both introduced in Section 2), to investigate the origins of shallow mesoscale (50–400 km) vertical motions in the trades. Specifically, we compare the simulated and observed mesoscale fluctuations of vertical velocity, virtual potential temperature and water vapor (Section 3). We present evidence that the mesoscale vertical motion observed in nature (a) does indeed develop in WTG balance, and (b) is remarkably well-simulated by the realistic LES. This will motivate us to evaluate the LES' mesoscale buoyancy budget, which reveals that the simulated vertical motions are driven by convective heating in precipitating shallow cumuli, at all scales between 12.5 and 400 km (Section 4). Hence, across the mesoscales, we should invert the canonical picture of vertical motion controlling the shallow convection.

To understand what controls the mesoscale vertical motion field, we must then understand what determines the variability in shallow convective heating. In Section 5, we discuss whether such variability is forced upon the trade-wind boundary layer, or if the circulations in turn affect the convection through the moisture field, establishing a two-way coupling akin to what is found in Bretherton and Blossey (2017)'s idealized LES. We find evidence for the latter, and end the paper by reviewing the implications for new conceptual sketches of the mesoscale trades (Section 6).

2. Simulation and Observation Data

2.1. Definitions

To more formally distinguish mesoscale variability in a variable ψ from larger- and smaller scale fluctuations, we separate ψ into averages over regions of (a) "small" scale (ψ_s, we take $\psi = \psi_s$), (b) "mesoscale" (ψ_m) and (c) "large" scale (ψ_l). Denoting spatial fluctuations around these averages with primes $'$, they relate to each other as

$$\psi = \psi_l + \psi'_m + \psi'_s = \psi_m + \psi'_s = \psi_s. \quad (1)$$

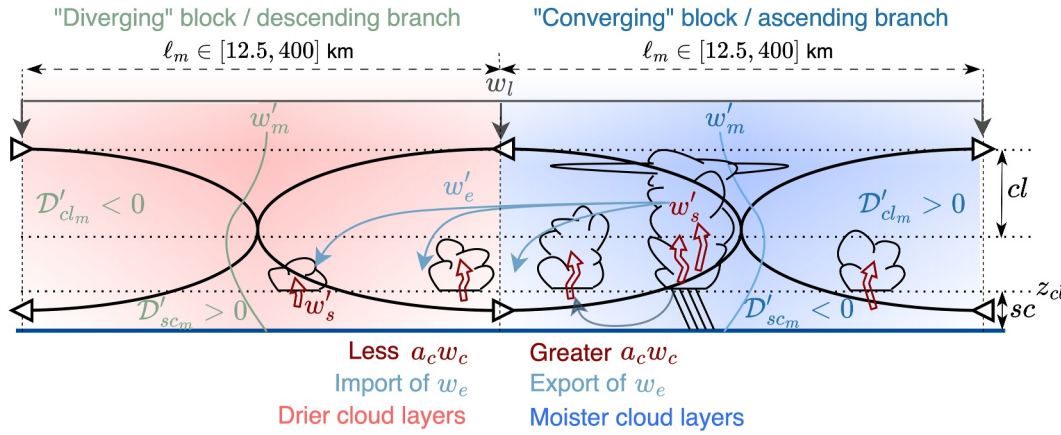

Figure 1. Conceptual illustration of a shallow circulation between mesoscale regions. A gentle large-scale descent aloft (w_l), is superimposed by mesoscale (ℓ_m) regions of subcloud-layer (sc) volume convergence $\mathcal{D}'_{sc_m} < 0$ and divergence $\mathcal{D}'_{sc_m} > 0$; these are the branches of coherent circulations which close in the upper cloud layer (cl), and whose vertical motion profiles are sketched as w'_m. Superimposed on these in turn is (small)-scale vertical motion in cumuli and turbulence w'_s. w'_m in ascending branches is carried by greater volume fluxes $a_{c_m} w_{c_m}$ through deeper, precipitating cumuli with a larger cloud-base cloud cover a_c, and by export of compensating environmental descent w_e toward descending branches with less strong $a_{c_m} w_{c_m}$. The export is achieved by gravity waves triggered by the additional convective heating in the ascending branches, working to keep the mesoscale in weak-temperature gradient balance. Ascending branches accumulate water vapor in their cloud layers (blue vs. red), potentially driving a self-reinforcing feedback that governs the life cycle of mesoscale shallow convection.

For $\psi = w$ (vertical velocity), Figure 1 indicates conceptually which features fall in each scale range. We will modify the scales to which ψ_l and ψ_m refer throughout the manuscript. Yet unless stated otherwise, ψ_m will refer to 200 km, and ψ_l to 400 km-scale averages; ψ'_s then refers to sub-200 km scale fluctuations. We will also approximate certain spatial fluctuations ψ' with temporal fluctuations ψ'' around temporal averages $\langle\psi\rangle$, which satisfy

$$\psi = \langle\psi\rangle + \psi''. \tag{2}$$

All these choices are practically motivated, as explained next.

2.2. ICON Large-Eddy Simulation

To interpret the shallow vertical motion observed during EUREC^{4}A, we will use the 41-day (10 January–20 February 2020) large-eddy simulations (LESs) of the campaign run with the Icosahedral Nonhydrostatic (ICON) model by Schulz and Stevens (2023, see their paper for further details). The simulation covers the North Atlantic between 60–47°W and 9–16.25°N at a horizontal grid spacing $\Delta x = 312$ m (ICON-312), and is forced by reanalysis and global modeling data. Specifically, the domain is subjected to horizontally and temporally varying sea-surface temperatures, and to variability in the flow across the lateral boundaries. A shorter simulation (1–7 February) over 59.75–50°W and 10.5–15.5°N at $\Delta x = 156$ m (ICON-156) returns similar statistics of 200-km scale cloud-base vertical motion (Figures S1–S2 in Supporting Information S1); we therefore choose to focus on the larger, longer ICON-312 simulation.

We analyze three-dimensional fields of specific humidity q_v, liquid cloud water specific humidity q_c, rain-water specific humidity q_r and virtual potential temperature θ_v (all as defined by Dipankar et al. (2015), who refer to θ_v as θ_ρ), their grid-resolved vertical fluxes, and the velocity field $u_j = [u,v,w] = [u_h,w]$, extracted from the ICON-312 simulation at its 3-hourly output frequency, and averaged over quadratic blocks of various sizes between 5 and 400 km to give ψ_m.

In contrast to LESs departing from spatially homogeneous conditions or kilometer-scale resolution mesoscale or global models, ICON-312 simultaneously represents synoptic variability, mesoscale processes and the large eddies of shallow convection. It also simulates longer time periods than other recent simulations of individual mesoscale weather events (Dauhut et al., 2023; Narenpitak et al., 2021; Saffin et al., 2023). Hence, the simulation

21698996, 2024, 18, Downloaded from https://agupubs.onlinelibrary.wiley.com/doi/10.1029/2024JD041417 by Technical University Delft, Wiley Online Library on [02/10/2024]. See the Terms and Conditions (https://onlinelibrary.wiley.com/terms-and-conditions) on Wiley Online Library for rules of use; OA articles are governed by the applicable Creative Commons License

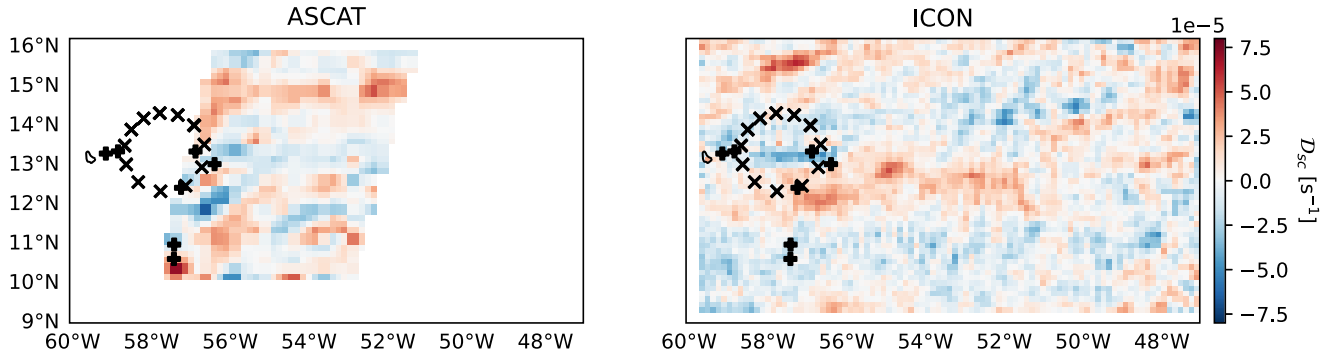

Figure 2. Fields of $\mathcal{D}_{sc}$ as estimated from ASCAT on 13 February 2020 at 14:15 UTC (left), and from the Icosahedral Nonhydrostatic (ICON) simulation at 15:00 UTC (right). The ICON data are coarse-grained to the roughly 25 km native resolution of ASCAT, and further smoothed to ASCAT's roughly 50 km effective resolution for $\mathcal{D}_{sc}$. Crosses and pluses indicate dropsonde launches from HALO and radiosonde launches in the sounding network, between 12:00 and 16:00 UTC, respectively.

allows both (a) comparisons against the observed statistics of mesoscale vertical motion during EUREC^{4}A (Bony et al., 2017), and (b) expansions of our view on the dominant mesoscale balances of shallow convection to the monthly time scale. Therefore, we analyze time-averaged statistics of ψ_m, and assume they sketch the climatological mesoscale cloud-circulation coupling in trade-wind regimes.

2.3. Observations

We construct statistics of w, q_v and θ_v observed during EUREC^{4}A from the "Joint Dropsonde Observations of the Atmosphere in Tropical North Atlantic Meso-scale Environments" (JOANNE, George, Stevens, Bony, Pincus et al., 2021), which aggregates dropsondes launched along 220-km diameter circles flown by the German High Altitude and Long range (HALO) research aircraft (Konow et al., 2021). This selects the default ψ_m scale of 200 km. Since JOANNE's circles only have a time dimension, we are forced to assume that its temporal fluctuations approximate spatial fluctuations. We follow George et al. (2023), and take ψ_m to be the average over three consecutively flown circles (roughly 3 hr), and assume ψ_m'' between such "circling sets" around the campaign-mean $\langle\psi\rangle$ can be reinterpreted as 200-km ψ_m'. Hence, we must assume temporal variability in larger-scale structures $\psi_l'' = 0$, which is often—but not always—tenable (Section 3).

Therefore, we supplement our time-varying dropsondes with temporally collocated soundings from a larger-scale spatial network of ships and a ground station (Stephan et al., 2020), as well as two spatially resolved products from daily overpasses of EUMETSAT's Metop-A satellite: (a) Profiles of q_v estimated by the Infrared Atmospheric Sounding Interferometer (IASI), and (b) 10 m wind speed and direction estimated by the Advanced Scatterometer (ASCAT). We use the level-2 Climate Data Record (CDR) IASI product (EUMETSAT, 2022), and the daily ASCAT-A CDR product gridded at 0.25° latitude and longitude (Ricciardulli & Wentz, 2016). We regrid the IASI retrievals, which are available on scan-lines perpendicular to the flight path, to the same 0.25° grid using nearest-neighbor interpolation. The ASCAT winds are converted to near-surface divergence $\mathcal{D}_{ns}$ using second order finite differences. Crucially, $\mathcal{D}_{ns}$ closely approximates the entire subcloud-layer average $\mathcal{D}_{sc}$, as we explore in detail in an upcoming companion manuscript. Hence, we can convert $\mathcal{D}_{ns}$ to cloud-base vertical motion w_{cb} using mass conservation in the Boussinesq limit:

$$w_{cb} = \mathcal{D}_{sc} z_{cb}. \tag{3}$$

With reference to Figure 1, we loosely define the subcloud layer to range between 0 and $z_{cb} = 600$ m. Figure 2 gives an impression of the retrieved $\mathcal{D}_{sc}$ variability on 13 February 2020 at 50 km scales, alongside its LES-derived complement.

Mirroring the LES, we average IASI and ASCAT data over square blocks. The largest scale we can attain for these satellite products is the average over the portion of a swath that intersects an analysis domain of 10–16° latitude, −60 to −50° longitude, in January and February 2020 (Figure 2). On average, this yields areas whose square root is roughly 400 km. This motivates our initial choice for ψ_l's scale.

21698996, 2024, 18, Downloaded from https://agupubs.onlinelibrary.wiley.com/doi/10.1029/2024JD041417 by Technical University Delft, Wiley Online Library on [02/10/2024]. See the Terms and Conditions (https://onlinelibrary.wiley.com/terms-and-conditions) on Wiley Online Library for rules of use; OA articles are governed by the applicable Creative Commons License

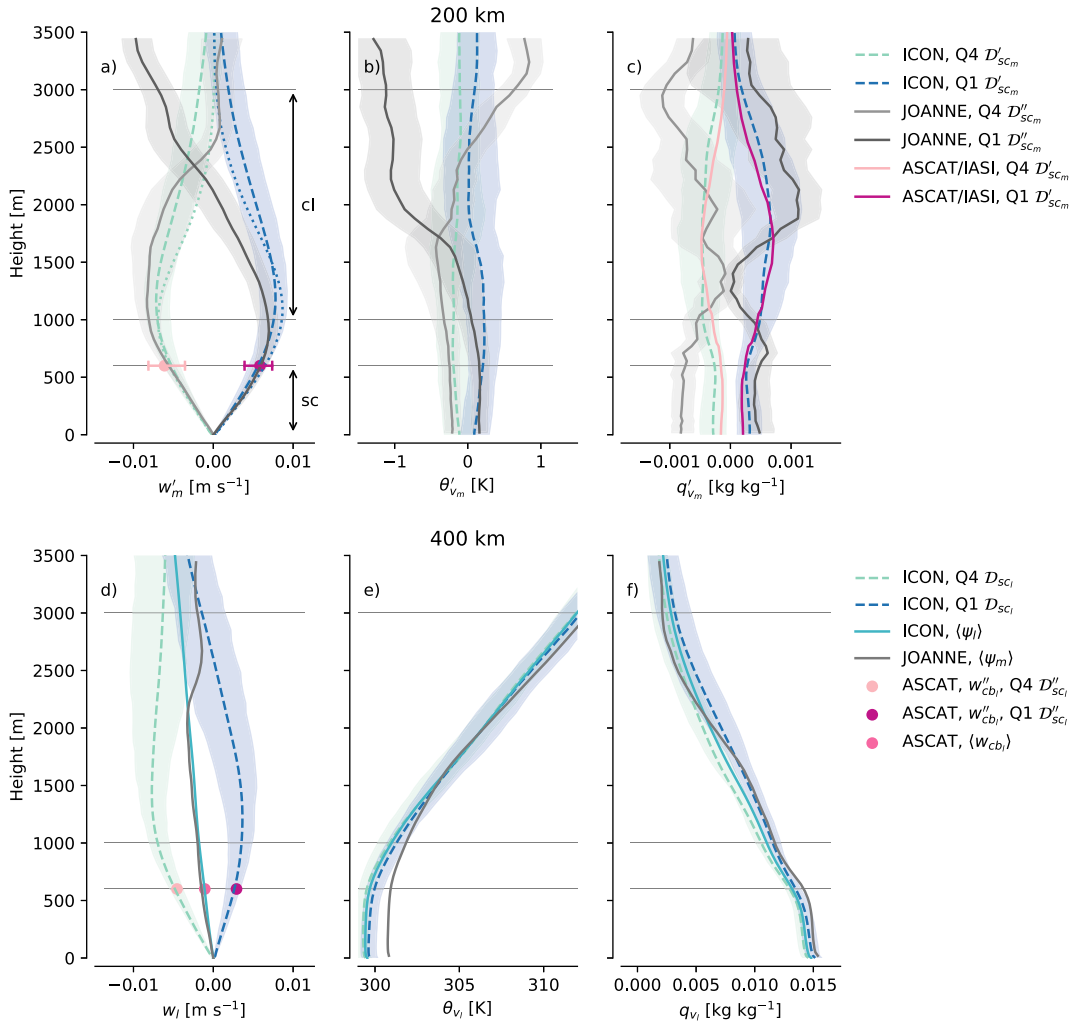

Figure 3. Spatial fluctuations of $\psi \in [w, \theta_v, q_v]$ (columns). Top row (a–c): Lowest (Q1) and highest (Q4) quartiles of 200 km-scale i) Icosahedral Nonhydrostatic (ICON) ψ'_m (Equation 1) sorted by $\mathcal{D}'_{sc_m}$, ii) JOANNE ψ''_m (Equation 2) sorted by circling-set averaged $\mathcal{D}_{sc}$ and iii) ASCAT w'_{cb_m} (Equation 3) and Infrared Atmospheric Sounding Interferometer (IASI) q'_{v_m}, sorted by ASCAT $\mathcal{D}'_{sc_m}$. Bottom row (d–f): Q1 and Q4 of 400 km-scale i) ICON ψ_l sorted by $\mathcal{D}_{sc_l}$ and ii) ASCAT w''_{cb_l} sorted by $\mathcal{D}''_{sc_l}$. Temporal campaign averages $\langle\psi_l\rangle$ (Equation 2) are included for all three data sets. Lines indicate time-averages of the Q1 and Q4 composites; shading indicates the interquartile range of temporal variability in ICON estimates of Q1 and Q4, and of 1,000 bootstrap estimates of Q1 and Q4 in JOANNE; horizontal whiskers indicate the same for ASCAT. Dotted lines in panel (a) show composites on ICON blocks which satisfy the shallow circulation criteria. The vertical extent of the layers used to define the subcloud-layer divergence $\mathcal{D}_{sc}$ and cloud-layer divergence $\mathcal{D}_{cl}$ are marked *sc* and *cl*, respectively.

Since IASI's vertical resolution is limited below 2 km altitude (EUMETSAT, 2021), it does not capture sharp features in the boundary layer's vertical structure, such as the trade inversion (Chazette et al., 2014; Menzel et al., 2018; Stevens et al., 2018). Yet, when compared to circle circumference-averaged values from JOANNE, IASI adequately captures variability of q_v over deeper layers, such as both the subcloud and cloud layers (Figure S3 in Supporting Information S1). Thus, we use the retrievals bearing their limitations in mind.

3. Mesoscale Vertical Motion and Weak Virtual Temperature Gradients

Figure 2 indicates that, in line with Bony and Stevens (2019); Stephan and Mariaccia (2021); George et al. (2023), both ASCAT and ICON feature a rich variability in shallow, mesoscale divergence patterns, of many scales. To quantify the dynamic and thermodynamic variability associated with these patterns, we composite the vertical structure of w, θ_v and q_v by quartiles of $\mathcal{D}_{sc}$ in blocks of the same scale (Figure 3). Here, we will first study w and θ_v; we return to the co-variability with q_v in Section 5.

21698996, 2024, 18, Downloaded from https://agupubs.onlinelibrary.wiley.com/doi/10.1029/2024JD041417 by Technical University Delft, Wiley Online Library on [02/10/2024]. See the Terms and Conditions (https://onlinelibrary.wiley.com/terms-and-conditions) on Wiley Online Library for rules of use; OA articles are governed by the applicable Creative Commons License

21698996, 2024, 18, Downloaded from https://agupubs.onlinelibrary.wiley.com/doi/10.1029/2024JD041417 by Technical University Delft, Wiley Online Library on [02/10/2024]. See the Terms and Conditions (https://onlinelibrary.wiley.com/terms-and-conditions) on Wiley Online Library for rules of use; OA articles are governed by the applicable Creative Commons License

At the 200 km scale, the depth and amplitude of JOANNE's w_m'', ASCAT's w'_{cb_m} and ICON's w'_m are remarkably consistent (Figure 3a, see also Figures S2–S3 in Supporting Information S1). Since ICON and ASCAT's spatial w'_m quartiles are robustly separated at any point in time during the campaign, we interpret this as evidence that the JOANNE-sensed w_m'' is truly spatial in nature, corroborating George et al. (2023)'s findings. In reanalysis data, George et al. (2023) find this spatial structure to characterize shallow circulations, defined by columns where $\mathcal{D}'_{sc_m}$ and its cloud-layer counterpart $\left(\mathcal{D}'_{cl_m}\right)$ have opposing sign. The same structure is evident also in the statistics of the LES in Figure 3a: Defining $\mathcal{D}'_{cl_m}$ in each 200×200 km^2 block by averaging $\mathcal{D}'_m$ over a layer spanning the upper cloud layer, inversion layer and lower free troposphere, $z_{cl} \in [1000, 3000]$ m (Figure 1), we find that blocks where $\mathcal{D}'_{cl_m}/\mathcal{D}'_{sc_m} < 0$ cover 59± 9% of the ICON domain. This matches George et al. (2023)'s reanalysis-derived coverage fractions of 58±7% very well. Additionally, 80% of the mesoscale columns with sub-cloud layer inflow and cloud-layer outflow border at least one column with a subcloud-layer outflow and cloud-layer inflow, or vice-versa. That is, ascending and descending branches of shallow circulations are spatially coherent at the mesoscale in ICON, as sketched in Figure 1. Finally, the vertical structure of w_m in mesoscale blocks where these criteria are satisfied (dotted lines in Figure 3a) is hardly distinguishable from that of all blocks. We conclude that the w'_m fields simulated by ICON embody the statistics of the mesoscale circulations observed in nature.

Averaged over larger scales (400 km ICON blocks; ASCAT swaths), the low-level vertical motion amplitudes $\left(w'_l\right)$ reduce in magnitude, but still vary substantially around the campaign-mean $\langle w_l \rangle$ (Figure 3d). Since $\langle w_l \rangle$ (approximated as $\langle w_m \rangle$ in JOANNE) does balance the climatological clear-sky radiative cooling measured above the boundary layer (George et al., 2023), these results indicate that 400 km is still too small a scale for w to represent adiabatic descent with the large-scale tropical circulation; it remains eclipsed by the mesoscale signal. We will estimate a different outer scale for w'_m in Section 4.4.

In spite of a cold and dry bias in θ_{v_l} and q_{v_l} (Figures 3e and 3f, further documented by Schulz and Stevens (2023)), ICON represents w'_m, w'_l and $\langle w_l \rangle$ very well. Therefore, we will use the simulation to explore the origins of the shallow mesoscale vertical motion. To do so, we exploit that circulations develop on top of very small mesoscale buoyancy fluctuations: Compositing θ'_{v_m} on $\mathcal{D}'_{sc_m}$ shows that θ'_{v_m} co-varies with the divergence patterns by only ~0.1 K across the campaign, underneath the trade inversion around 1,500 m, both in ICON and in JOANNE (Figures 3b and e). Above 1,500 m, JOANNE's θ''_{v_m} grows to around 1 K. However, this variability is also present in the larger-scale sounding network (Figure S4 in Supporting Information S1). That is, JOANNE's larger free-tropospheric θ''_{v_m} appears to embody larger-scale, temporal variability in the lapse rate; spatial mesoscale buoyancy anomalies remain small. Also the heating rates $\partial_t \theta_v$, as far as we can estimate them, are similar between JOANNE's mesoscale circles and the larger-scale sounding network (Figure S5 in Supporting Information S1). In all, while the scarcity of the observational data poses limits to the strength of our conclusions, the data we do have supports the use of WTG as a useful starting point for conceptual models of shallow vertical motion in the trades.

4. Shallow Circulations Anchored in Precipitating Shallow Convection

4.1. Mesoscale Buoyancy Budget

To formulate a WTG model, we will concentrate on the budget for θ_v, which is conserved by ICON, with two approximations. First, we treat the equation in the anelastic limit, since we consider shallow convective and internal wave phenomena over horizontal scales where sound waves may still be considered fast (e.g., R. Klein, 2010). Second, we approximate θ_v with the "liquid-water virtual potential temperature" θ_{lv}, which approximately satisfies:

$$\theta_{lv} \approx \theta_v - \left(\frac{L_v}{c_p \Pi \Theta} - \frac{R_v}{R_d}\right)\Theta\left(q_c + q_r\right) = \theta_v - a_3 \Theta\left(q_c + q_r\right). \tag{4}$$

L_v is the latent heat of vaporization, c_p is the specific heat of dry air at constant pressure, $\Pi = \left(p/p_0\right)^{R_d/c_p}$ is the Exner function where p_0 denotes a reference pressure and R_d the gas constant of dry air, R_v is the gas constant for water vapor and Θ is a reference potential temperature scale of the boundary layer (taken to be 300 K). These variable choices identify the constant $a_3 \approx 7$, adopted from Stevens (2007)'s Equation 10. θ_{lv} has the advantage over θ_v that it is conserved over reversible condensation and evaporation, yet when fluctuations in q_c and q_r are small or stationary, θ'_{lv} approximates the buoyancy or its tendency very well. Additionally, its vertical flux

21698996, 2024, 18, Downloaded from https://agupubs.onlinelibrary.wiley.com/doi/10.1029/2024JD041417 by Technical University Delft, Wiley Online Library on [02/10/2024]. See the Terms and Conditions (https://onlinelibrary.wiley.com/terms-and-conditions) on Wiley Online Library for rules of use; OA articles are governed by the applicable Creative Commons License

convergence closely tracks the work done by condensational heating in non-precipitating shallow cumuli (Stevens, 2007), and mesoscale fluctuations therein (Bretherton & Blossey, 2017; Janssens et al., 2023). The budget for θ_{lv} reads:

$$\partial_t \theta_{lv} = -\partial_x (u_h \theta_{lv}) - \frac{1}{\rho_0}\partial_z \left(\rho_0 w \theta_{lv}\right) - \frac{1}{\rho_0 c_p \Pi}\partial_z (\mu L_v P + R), \tag{5}$$

where ρ_0 is the reference density required to satisfy the equation in the anelastic limit, and ∂_t, ∂_x and ∂_z refer to differentiation in the temporal, the two horizontal and the vertical dimension, respectively. Two diabatic source terms appear: The convergence of (a) radiative fluxes R, and (b) warm precipitation fluxes P, scaled by the parameter

$$\mu = 1 - \frac{0.608 c_p \Pi \Theta}{L_v} \approx 0.93, \tag{6}$$

following, for example, Bretherton and Wyant (1997). Using the definition Equation 1 and the anelastic equation of mass conservation, Equation 5 can be rewritten into a relation for θ'_{lv_m}:

$$\begin{aligned}
&\underbrace{\partial_t \theta'_{lv_m} + u_{h_l} \partial_x \theta'_{lv_m}}_{1} = \underbrace{-u'_{h_m} \partial_x \theta_{lv_l}}_{2} \underbrace{- w_l \partial_z \theta'_{lv_m}}_{3} \underbrace{- w'_m \partial_z \theta_{lv_l}}_{4} \\
&\underbrace{- \partial_x \left[u'_{h_m} \theta'_{lv_m} - \left(u'_{h_m} \theta'_{lv_m}\right)_l\right]}_{5} \underbrace{- \partial_x \left[\left(u'_{h_s} \theta'_{lv_s}\right)_m - \left(u'_{h_s} \theta'_{lv_s}\right)_l\right]}_{6} \\
&\underbrace{- \frac{1}{\rho_0}\partial_z \left[\rho_0 \left(w'_m \theta'_{lv_m} - \left(w'_m \theta'_{lv_m}\right)_l\right)\right]}_{7} \underbrace{- \frac{1}{\rho_0}\partial_z \left[\rho_0 \left(\left(w'_s \theta'_{lv_s}\right)_m - \left(w'_s \theta'_{lv_s}\right)_l\right)\right]}_{8} \\
&- \frac{1}{\rho_0 c_p \Pi}\partial_z \left(\mu L_v P'_m + R'_m\right)
\end{aligned} \tag{7}$$

We estimate term 1 (storage) by taking the difference between a block's θ'_{lv_m} at time t, and the θ'_{lv_m} of the block which resides $u_{h_l}\Delta t$ upstream at time $t - \Delta t$, with $\Delta t = 3$ hr. We ignore terms 2, 3, 5, 6 and 7, as both scale analysis and actually evaluating these terms revealed them to generally be an order of magnitude smaller than the leading-order terms in the balance. This leaves terms 4 (mesoscale vertical advection) and 8 (anomalous vertical flux convergence), and the two diabatic sources.

R'_m is computed from fields of radiative heating rates, which are stored by the model once each simulated day, usually after sunset. Hence, it comprises longwave cooling only, and can be evaluated at 1/8th the frequency of the advective terms. P'_m imprints itself on the θ'_{lv_m} budget by sedimenting q_r and q_c with respect to the local flow. We compute it by reproducing ICON's rain sedimentation scheme (based on Stevens & Seifert, 2008) offline, using fields of q_r, q_c, ρ and the rain-droplet number concentration n_r, which are also stored once a day. At time steps where P and R are not available, we approximate P from offline calculations of the autoconversion and accretion rates, following Radtke et al. (2023) (see Text S1 in Supporting Information S1), and we ignore R, for reasons that will shortly become clear. The budget terms are composited by the first and fourth quartiles (Q1, Q4) of $\mathcal{D}'_{sc_m}$ in 200 km blocks, and averaged over the 2-month simulation period. The results are plotted in Figure 4.

Evaluating the budget leaves a small residual, which may derive from a combination of the following: (a) The small budget contributions we have ignored, (b) numerical errors in our central difference approximations of (i) tendencies over the 3 hr time intervals that the ICON data is stored at and (ii) horizontal gradients over 200 km m-blocks, (c) errors in our computation of P'_m, and (d) the missing sub-grid contributions to $\left(w'_s \theta'_{lv_s}\right)$). Nevertheless, a few salient features robustly emerge. The total storage of θ'_{lv_m} in 200 km blocks that follow the l-scale flow (term 1) is smaller than 1 K day^{-1}, in both converging and diverging regions. This compares well to the daily-averaged heating rate differences between JOANNE's 200 km circles and the larger-scale sounding network (Figure S5 in Supporting Information S1). In ascending regions, we observe anomalous convergence of θ_{lv}, supported primarily

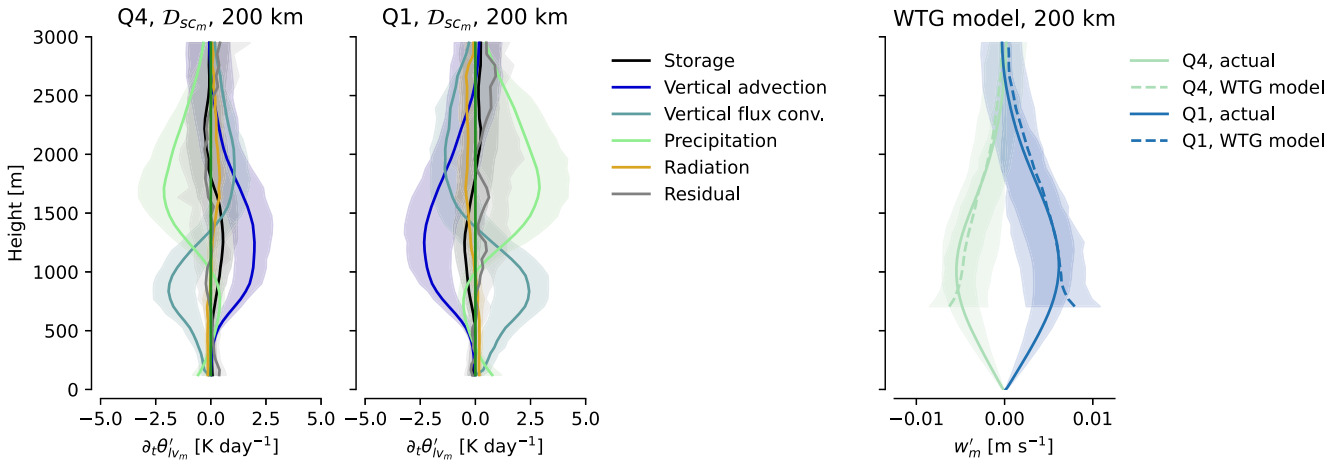

Figure 4. Left and central columns: Budgets of θ'_{lv_m} averaged over the entire simulation period, in 200 km blocks, composited by $\mathcal{D}'_{sc_m}$ (Q4 and Q1), as in Figure 3. Right column: w'_m as diagnosed directly from the simulations (unbroken lines, "actual"), and from the Weak Temperature Gradient model for w'_m (Equation 8), plotted only above 700 m where gradients in θ_v become appreciable. Shading captures the temporal interquartile range.

by additional condensation and liquid-water transport through cumulus clouds, up to the inversion base around 1,500 m. In the inversion layer and lower free troposphere, anomalous latent heating driven by precipitation takes over, while the remaining liquid water evaporates, generating anomalous cooling. Together, these two θ_{lv} sources (henceforth referred to as convective heating) balance adiabatic cooling from mesoscale ascent along the large-scale stratification. Q4 experiences largely the opposite situation; its convective heating anomalies are smaller than the large-scale average, balancing $w'_m < 0$.

Presenting a balanced budget is insufficient for a dynamical description of which term causes another to respond. However, WTG relies on a well-established principle that does imply causality. The cloud layer, inversion layer and free troposphere of our simulations are all stably stratified, with a Brunt-Väisälä frequency $N \approx 0.014\ \mathrm{s}^{-1}$. In such stably stratified layers, convective heating causes buoyancy fluctuations, which are rapidly distributed horizontally by gravity waves. This prevents θ'_v between a collection of active cumuli and their environment from growing beyond the adjustment time scale of the waves, over the horizontal area they reach (Bretherton & Blossey, 2017; Bretherton & Smolarkiewicz, 1989; Sobel et al., 2001). For our N and the first vertical half-wavelength of our heating anomaly ($h_w \approx 2{,}500$ m), these waves propagate horizontally at roughly $c \approx Nh_w/\pi \approx 12\ \mathrm{m\,s}^{-1}$; that is, the first wave mode spreading uniformly in all directions would relax θ'_{v_m} to zero over a 200 km region over a time scale of less than 3 hr. Instead of raising θ'_v, the θ'_v sources cause a collective vertical motion over such areas, as discussed further in Section 4.3; the adiabatic cooling with this motion balances the budget.

In all, we may simplify Equation 7 to a reasonable model of w'_m (right column, Figure 4):

$$w'_m \approx -\left(\frac{1}{\rho_0}\partial_z\left(\rho_0 F_{\theta'_{lv_m}}\right) + \frac{1}{\rho_0 c_p \Pi}\partial_z\left(\mu L_v P'_m\right)\right)/\partial_z\theta_{lv_l} \tag{8}$$

Where

$$F_{\theta'_{lv_m}} = \left(w'_s\theta'_{lv_s}\right)_m - \left(w'_s\theta'_{lv_s}\right)_l. \tag{9}$$

This model holds well above the height where θ_{lv_l} becomes stably stratified, around 700 m (right column of Figure 4). Below this height, Equation 8 diverges as $\partial_z\theta_{lv_l} \to 0$, reflecting the WTG approximation's inability to predict w'_m beyond the vertical level where the heat source acts (Romps, 2012a). Instead, one commonly assumes that w'_m returns linearly to zero at the surface (Daleu et al., 2015; Raymond & Zeng, 2005; Sobel & Bretherton, 2000), which Figure 3 supports. We could alleviate this ad-hoc approximation by analyzing the equations in a damped-gravity wave framework (e.g., Kuang, 2008; Romps, 2012b). We still present our results in the WTG approximation, because it shows most directly that the buoyancy source anomaly driving the circulations is

21698996, 2024, 18, Downloaded from https://agupubs.onlinelibrary.wiley.com/doi/10.1029/2024JD041417 by Technical University Delft, Wiley Online Library on [02/10/2024]. See the Terms and Conditions (https://onlinelibrary.wiley.com/terms-and-conditions) on Wiley Online Library for rules of use; OA articles are governed by the applicable Creative Commons License

21698996, 2024, 18, Downloaded from https://agupubs.onlinelibrary.wiley.com/doi/10.1029/2024JD041417 by Technical University Delft, Wiley Online Library on [02/10/2024]. See the Terms and Conditions (https://onlinelibrary.wiley.com/terms-and-conditions) on Wiley Online Library for rules of use; OA articles are governed by the applicable Creative Commons License

situated in the cloud layer (Figure 4); the sub-cloud layer must adjust to the subsequent vertical pressure gradient by also ascending or descending adiabatically (Romps, 2012b). Thus, at 200 km scales, and over a whole month of trade-wind weather (denoted by the shading in Figure 4), the vertical profile of w'_m balances the production of mesoscale buoyancy fluctuations by heating in mesoscale patterns of shallow, precipitating convection.

4.2. Lacking Mesoscale Radiative Cooling Anomalies

It is noteworthy that we obtain an accurate model for w'_m (Equation 8) without including mesoscale radiative heating anomalies: Its contributions to the θ'_{lv_m} budget are negligible (golden lines in Figure 4). These results run counter to the idea that the anomalous q'_{v_m} associated with the circulations (Figures 3c and 3f) would result in a horizontal radiative cooling differential, which could feed back on and strengthen the circulations. Such an effect is thought to be key for the self-aggregation of deep convection in cloud-resolving models (e.g., Muller et al., 2022, and references therein), and has been suggested to be sufficiently potent to drive shallow circulations in the subtropics too (Naumann et al., 2017, 2019; Prange et al., 2023; Schulz & Stevens, 2018; Stevens et al., 2018). Yet, our results, the simulations by Bretherton and Blossey (2017) and EUREC^{4}A observations (George et al., 2023) all indicate that there is no relationship between mesoscale radiative heating anomalies, and mesoscale vertical motion.

If anything, we find small radiative cooling in converging regions (Figure 4 central panels). This might more readily trigger convection, and thus feed back on the circulations through additional convective heating. Such cooling may especially be found across large cloud anvils, which ICON lacks (Schulz & Stevens, 2023), and off cloud sides (Klinger et al., 2017), which is a 3D effect that ICON does not simulate. Furthermore, the ICON simulations lack the elevated moist layers sensed by JOANNE (Figure 3c), which may enhance horizontal radiative cooling contrasts (Fildier et al., 2023; Prange et al., 2023). Finally, variability in large-scale radiative cooling, through the diurnal cycle or from larger moisture features, is key to set the large-scale convective adjustment (Betts & Ridgway, 1988). On the 12-hr scale of a night, such large-scale increases in convection might well disproportionately affect regions which are already convecting, and thus amplify existing circulations (Vial et al., 2021; Janssens, 2023, ch. 7). Hence, while mesoscale radiative cooling patterns should be abandoned as a direct explanation of w'_m in the trades, there are still lessons to learn about the role of radiation in the mesoscale cloud-circulation coupling.

4.3. Mass Fluxes, Compensating Subsidence and Variability in Active Cloudiness

Where in a mesoscale block does shallow, mesoscale ascent or descent take place, and how does it relate to shallow cloudiness? To answer this, we decompose w_m into the vertical motion w_{c_m} averaged over a mesoscale block's cloudy area fraction a_{c_m}, and the vertical motion in the environment w_{e_m}. $a_{c_m} w_{c_m}$ is the cloud-conditioned volume flux, which in the anelastic limit varies horizontally in proportion with the mass flux. At 970 m altitude, where w_m reaches its maximum (Figure 3), mass conservation for a 200 km block then demands

$$w_m = a_{c_m} w_{c_m} + (1 - a_{c_m})\, w_{e_m}, \tag{10}$$

Figure 5a) displays both contributions to w_m, binned by w_m itself. It shows that spatial variability in w_m is due primarily to variability in the ascent within cumulus clouds ($a_{c_m} w_{c_m}$, dark blue line), because this ascent does not need to balance the compensating subsidence in cloud-free regions ($(1 - a_{c_m})\, w_{e_m}$, light blue line) within a mesoscale block. The WTG framing suggests why: The spectrum of gravity waves triggered by the heating in cumuli with upward mass fluxes rapidly carry the mass fluxes' compensating subsidence beyond a 200 km block boundary (Bretherton & Smolarkiewicz, 1989; Mapes, 1993; Nicholls et al., 1991). When $a_{c_m} w_{c_m}$ varies between mesoscale blocks, blocks with smaller $a_{c_m} w_{c_m}$ have less convective heating (Q4 vs. Q1 panels in Figure 4), and trigger waves of smaller depth and amplitude than blocks with larger $a_{c_m} w_{c_m}$. Hence, they are unable to export the same amount of compensating subsidence as they receive, and become reservoirs of environmental descent, as we observe at $w_m < 0$, where $a_{c_m} w_{c_m}$ almost returns to zero, and $w_m \approx (1 - a_{c_m})\, w_{e_m}$.

Our results harmonize with other EUREC^{4}A observations (Vogel et al., 2022), which show that mesoscale variations in $a_c w_c$ co-vary strongly with w_m at cloud base. In fact, the subcloud-layer mass budget which Vogel et al. (2022) solve to diagnose balances between $a_{c_m} w_{c_m}$, $(1 - a_{c_m})\, w_{e_m}$ (interpreted as an entrainment velocity) and

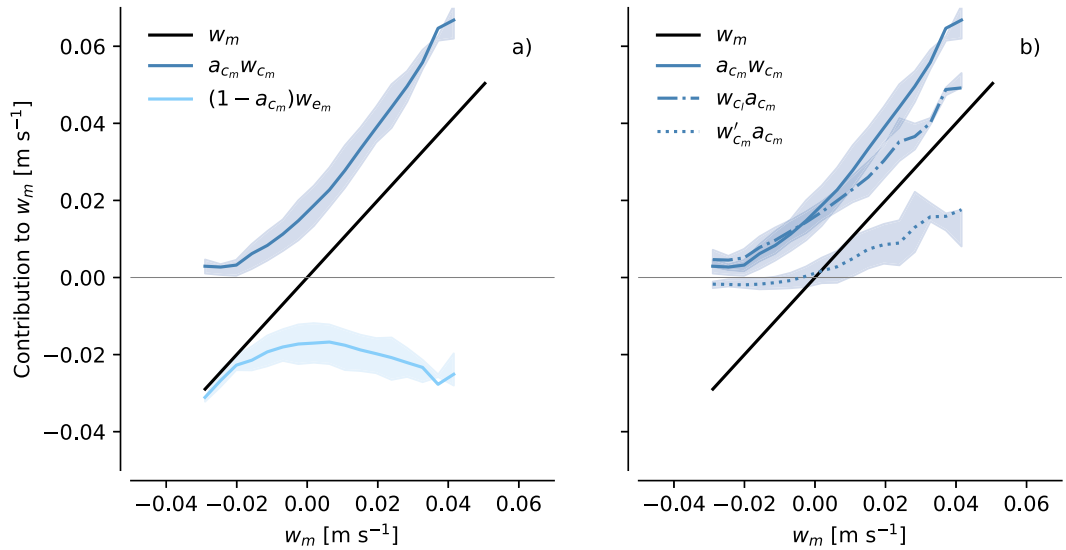

Figure 5. 200 km-scale w_m at a height of 970 m diagnosed in the simulation, broken down at each w_m according to Equation 10 (a), and Equation 11 (b). Shading indicates the temporal interquartile range.

w_m (their Equation 1), is conceptually indistinguishable from our Equation 8 evaluated at cloud base and partitioned according to Equation 10 (Stevens, 2006; Vilà-Guerau De Arellano et al., 2015), if $\partial_z P'_m$ is small. This latter assumption appears to hold well at cloud base in both observations (Albright et al., 2022) and the LES (Figure 4).

Variability in $a_{c_m}w_{c_m}$ can express itself both through variability in the cloud fraction itself at a horizontally constant mean ascent through clouds (i.e., a large-scale average, w_{c_l}), and (b) through horizontal (co-)variability of a_{c_m} with fluctuations around w_{c_l}, w'_{c_m}. George, Stevens, Bony, Klingebiel, and Vogel (2021) and Vogel et al. (2022) find that this decomposition approximately reduces to

$$a_{c_m}w_{c_m} = a_{c_m}w_{c_l} + a_{c_m}w'_{c_m} \approx a_{c_m}w_{c_l}, \tag{11}$$

that is, that stronger mass fluxes are due to increases in a_c, while $w_{c_m} \approx w_{c_l}$. In Figure 5b), we decompose $a_{c_m}w_{c_m}$ according to Equation 11 in the ICON simulation. It agrees with earlier observations that increases in $a_{c_m}w_{c_m}$ are primarily related to variability in a_{c_m} (Klingebiel et al., 2021; Lamer et al., 2015; Sakradzija & Klingebiel, 2020), though variability in w_{c_m} cannot be neglected in areas of strong mesoscale ascent. The classical picture of trade-wind cloud-circulation coupling would then suggest that w_m controls the cloud fraction in the trades. It is likely that w_m affects the cloudiness (Section 5), but WTG physics emphasize that it cannot be the only direction in the relationship: In the cloud layer, w'_m results primarily from the mesoscale variability in the fraction of active cumulus clouds.

4.4. Cloud-Layer Vertical Motion Variability Across the Mesoscales

Does convective heating variability drive circulations also at other scales than the 200 km scale analyzed thus far? To answer this question, we expand our simulation-observation comparison and WTG analysis to the full spatial scale ranges represented by ICON and ASCAT. Specifically, we compute w_m and its WTG approximation over block sizes $\ell_m \in [5-800]$ km in ICON, and $\ell_m \in [25-400]$ km in ASCAT, and take the standard deviation σ_w at each scale, at a height of 970 m. Figure 6 shows that in ICON, these vertical motion amplitudes reduce as $\sigma_w(\ell_m) \sim \ell_m^{-1}$ for $\ell_m \in [5-40]$ km, as $\sigma_w(\ell_m) \sim \ell_m^{-\frac{1}{2}}$ for $\ell_m \in [40-300]$ km, and again as ℓ_m^{-1} at the largest scales. The results are in close agreement with ASCAT estimates (square pink blocks), with the ℓ^{-1} scaling of divergence amplitudes in the EUREC^{4}A sounding network found by Stephan and Mariaccia (2021), with the vertical motion contained only in blocks satisfying the SMOC criteria (dotted lines), and with the predictions from the WTG model Equation 8 for $\ell \in [12.5-400]$ km (crosses). That is, we may consider the cloud-layer vertical

21698996, 2024, 18, Downloaded from https://agupubs.onlinelibrary.wiley.com/doi/10.1029/2024JD041417 by Technical University Delft, Wiley Online Library on [02/10/2024]. See the Terms and Conditions (https://onlinelibrary.wiley.com/terms-and-conditions) on Wiley Online Library for rules of use; OA articles are governed by the applicable Creative Commons License

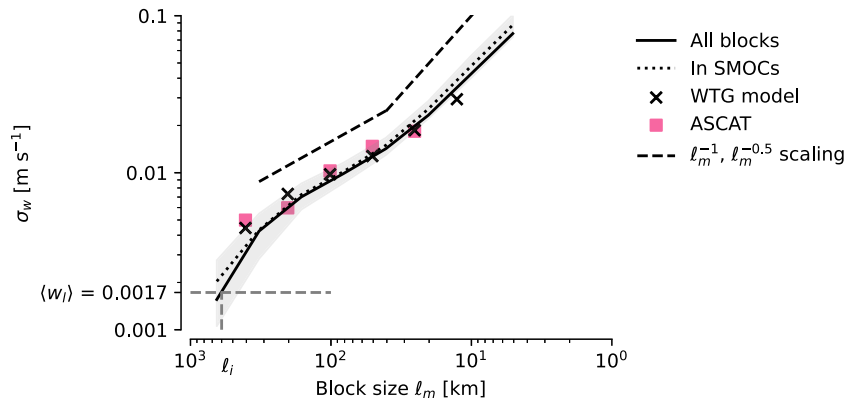

Figure 6. Variability in w_m as a function of block size ℓ_m at a height of 970 m ($\sigma_w(\ell)$), computed in the simulation over all blocks (unbroken line), blocks belonging to Shallow Mesoscale Overturning Circulations (dotted line) and estimated using the Weak Temperature Gradient balance Equation 8 (crosses). σ_w estimated from ASCAT is indicated in pink squares. The campaign-mean vertical motion $\langle w_l \rangle$ and its intersection scale ℓ_i are indicated by broken gray lines, while the other broken lines illustrate scaling as ℓ_m^{-1} and $\ell_m^{-\frac{1}{2}}$. Shading indicates the temporal interquartile range of σ_w at each scale.

motion in the trades to be the ever-weakening imprint of shallow convective thermal forcing across the mesoscales.

Only at 700 km does σ_w reduce below the magnitude of $\langle w_l \rangle$ (horizontal line in Figure 6), the campaign-averaged vertical motion (Figure 3d). Below this intersection scale ℓ_i, divergence in the shallow cloud layer is dominated by the signal of mesoscale circulations, and only above it does one recover the canonical large-scale subsidence. ℓ_i is affected by the dropoff in σ_w at the largest scales of the limited-area simulation, which may be a truncation effect. Hence, ℓ_i could be even larger. Yet, $\ell_i \approx 700$ km closely matches the decorrelation length in w calculated from a previous ICON simulation by Bony and Stevens (2019). We therefore suggest that one may interpret 700 km as a conservative estimate for the upper boundary to the non-divergent, mesoscale flow.

5. Discussion: What Controls Mesoscale Patterns of Shallow Convective Heating?

If shallow convective heating is necessary to produce shallow mesoscale vertical motions in the trades, then what sets the mesoscale shallow convection patterns? Many mesoscale forcings on the convection (e.g., Aemisegger et al., 2021; Chen et al., 2023; Stephan & Mariaccia, 2021) and feedbacks between the convection and the circulations (e.g., Dixit et al., 2021; Radtke et al., 2022; Seifert et al., 2015) might play a role, and we leave it to future work to comprehensively assess these. To give direction to such studies, here we discuss two plausible mechanisms: Surface-driven forcing and a moisture-convection feedback.

Mesoscale circulations may be driven by surface forcing patterns through mesoscale variations in the sea-surface temperatures or near-surface winds, which will drive commensurate variations in the surface buoyancy flux $\left(w'\theta'_{lv}\right)_{m,0}$ (Acquistapace et al., 2022; Chen et al., 2023; Park et al., 2006). One would expect the convergence of $\left(w'\theta'_{lv}\right)$ throughout the subcloud- and cloud-layers to adjust to these changes within an eddy-turnover time (e.g., Bellon & Stevens, 2013; Bretherton & Park, 2008; Stevens, 2007), leading to convective heating fluctuations atop the warm anomalies that could rapidly translate to w'_m.

We may also anticipate a moisture-convection feedback because (a) in case study simulations, shallow circulations drive the aggregation of moisture into regions that are already moist (Bretherton & Blossey, 2017; Narenpitak et al., 2021; Saffin et al., 2023), and (b) given WTG, moister regions are expected to convect more readily than drier regions, further strengthening the circulations. Figure 3c) confirms that in all our data sets, the ascending branches of circulations occur in moist columns, and the descending branches in dry columns. There are also many theories that suggest how moist anomalies could stimulate convective heating: They could prevent entrainment drying (George et al., 2023; Janssens et al., 2023), trigger more convection by raising the column moist-static energy (Bretherton & Blossey, 2017) or encourage precipitation (Nuijens et al., 2009; Radtke

21698996, 2024, 18, Downloaded from https://agupubs.onlinelibrary.wiley.com/doi/10.1029/2024JD041417 by Technical University Delft, Wiley Online Library on [02/10/2024]. See the Terms and Conditions (https://onlinelibrary.wiley.com/terms-and-conditions) on Wiley Online Library for rules of use; OA articles are governed by the applicable Creative Commons License

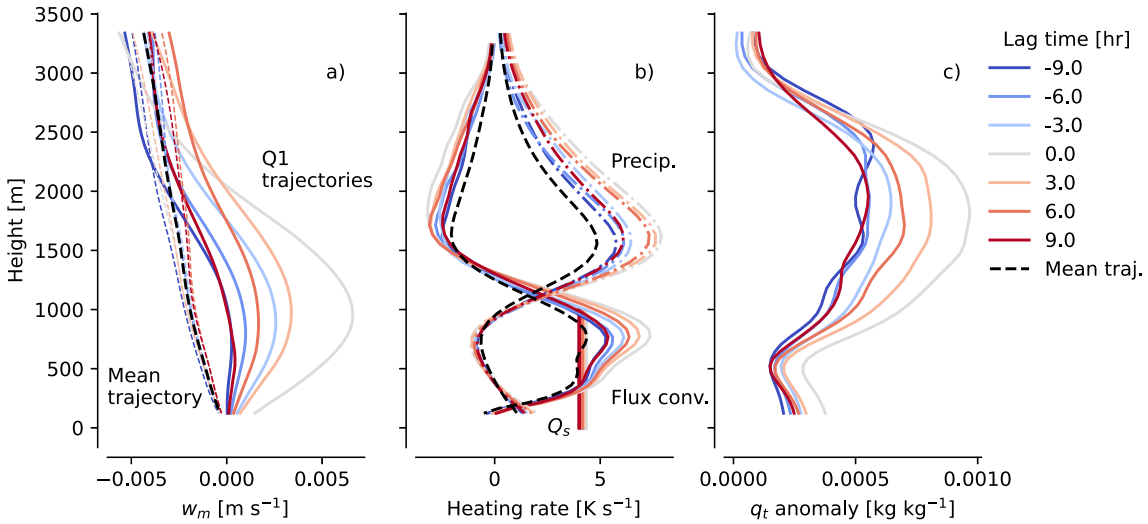

Figure 7. Profiles along Lagrangian trajectories characterizing the evolution in the quartile of 200 km blocks with the strongest $\mathcal{D}_{sc_m}$ at zero lag, traced from 9 hr lead to 9 hr lag times along Lagrangian trajectories through the Icosahedral Nonhydrostatic Large-Eddy Simulation. (a) Vertical motion, where unbroken lines indicate trajectories along Q1 blocks, dotted lines indicate the evolution along the mean over all blocks, and black, broken lines represent the time-average over an average trajectory; (b) θ_{lv_m} heating rates from Equation 8, decomposed into contributions from the convergence of $\left(w'\theta'_{lv}\right)_m$ (unbroken lines) and P_m (dash-dotted lines), and the evolution of the surface-controlled heating Q_s (vertical lines, Equation 12); (c) q_t anomaly in Q1 trajectories with respect to a mean trajectory. All profiles are averaged over the 79 launch times.

et al., 2023), in turn driving direct latent heating (Figure 4) or the formation of cold pools which can further sustain convection (Dauhut, personal comm.; Alinaghi et al., 2024). Yet we cannot here conclude which, if any, of these processes translate moisture to convection, because (a) we do not have the data to trace individual convective elements through their simulated moisture anomalies, and (b) we cannot confirm whether those moisture anomalies in nature primarily inhabit the converging regions' cloud layers, as indicated by ICON and the IASI-ASCAT composites, or the subcloud layer, as indicated by JOANNE (Figure 3c). While we believe this difference is partially due to the order of magnitude fewer data points in JOANNE, resolving it demands more work. Instead, we therefore concentrate on understanding how the shallow circulations influence moisture anomalies.

To do so, we trace the time-evolution of 200 km blocks along Lagrangian trajectories with the 200 km-scale horizontal velocity at a height of 1,500 m. We extract trajectories from ICON through successive 3-hourly first-order backwards finite differences (into the past) and forwards differences (into the future), launched from all 200 km blocks in the domain, at local noon and midnight. This gives us 448 trajectories at 79 launch times. We stop tracing each trajectory at a lead and lag time of 9 hr, or when the domain boundary is encountered, and assume these trajectories track coherent air masses, following for example, Eastman et al. (2021), Lewis et al. (2023), Saffin et al. (2023). At each launch time, we extract the quartile of trajectories with the largest $-\mathcal{D}_{sc_m}$ (Q1 $\mathcal{D}'_{sc_m}$), and the mean trajectory. Figure 7a shows the evolution of both Q1 w_m (unbroken lines) and the mean w_m (dotted lines), averaged over all launch times.

With respect to the mean w_m, Q1 blocks possess anomalous cloud-layer ascent already at 9 hr lead times. Over the following 18 hr, w_m robustly amplifies and decays around its zero-lag peak (gray line, corresponding to ICON Q1 in Figures 3a and 4). Throughout the strengthening phase of its life cycle, Q1 w_m remains balanced by a growing heat flux convergence and latent heating, plotted in Figure 7b. That is, the WTG model Equation 8 holds along a trajectory, suggesting that radiative heating anomalies also do not play a meaningful role in the development of 200 km-scale w_m, although (a) we do not have radiative heating rates from the LES to assess this explicitly, and (b) we cannot rule out that radiative contrasts do matter in specific situations, for example, for larger "Fish" structures (Fildier et al., 2023). The evolution of w_m also is not meaningfully different between trajectories launched during daytime or during nighttime (not shown), but it is sensitive to the chosen (200 km) scale; smaller anomalies develop and decay faster. Hence, the following results are specific to 200 km scale structures, and may differ for structures of different size.

21698996, 2024, 18, Downloaded from https://agupubs.onlinelibrary.wiley.com/doi/10.1029/2024JD041417 by Technical University Delft, Wiley Online Library on [02/10/2024]. See the Terms and Conditions (https://onlinelibrary.wiley.com/terms-and-conditions) on Wiley Online Library for rules of use; OA articles are governed by the applicable Creative Commons License

21698996, 2024, 18, Downloaded from https://agupubs.onlinelibrary.wiley.com/doi/10.1029/2024JD041417 by Technical University Delft, Wiley Online Library on [02/10/2024]. See the Terms and Conditions (https://onlinelibrary.wiley.com/terms-and-conditions) on Wiley Online Library for rules of use; OA articles are governed by the applicable Creative Commons License

5.1. Surface Buoyancy Flux Forcing

Is the increasing convective heating controlled by mesoscale surface forcing? We estimate this by computing the buoyancy flux convergence through the subcloud layer

$$Q_s = -\frac{\left(w'\theta'_{lv}\right)_{m,z_{cb}} - \left(w'\theta'_{lv}\right)_{m,0}}{z_{cb}}. \tag{12}$$

Since the cloud-base buoyancy flux $\left(w'\theta'_{lv}\right)_{m,z_{cb}}$ can be well-explained by the surface flux $\left(w'\theta'_{lv}\right)_{m,0}$ (e.g., Albright et al., 2022; Lilly, 1968), Q_s represents the surface-controlled heating rate. Hence, if Q_s (vertical lines in Figure 7b) can also describe the evolution of the *cloud-layer* convergence of anomalous heat fluxes along Q1 trajectories, w'_m would be surface-controlled.

Indeed, Q_s explains the resolved flux convergence throughout the sub-cloud and cloud layers averaged over a mean trajectory (black dashed lines), as assumed in most classical theory and shallow convection parameterizations (e.g., Bretherton & Park, 2009). However, in Q1 blocks, the cloud-layer convergence of $\left(w'\theta'_{lv}\right)_m$ far exceeds the quasi-stationary Q_s; so does the precipitation-driven latent heating. Hence, the growth of the cloud-layer heating and w_m cannot be explained by rapid convective adjustment to surface buoyancy flux anomalies, as would be expected if w_m were driven by mesoscale SST anomalies. Most likely, these SST anomalies are simply too weak (~0.2 K) to leave a first-order imprint on the mesoscale vertical motion field, and they might re-emerge as a more important driver in regions where mesoscale SST gradients are larger.

5.2. Evolution of Moist Anomalies

So does the growth of w_m instead develop together with moist anomalies? Figure 7c shows that Q1 trajectories possess anomalously moist cloud layers compared to an average trajectory already 9 hr before the convection peaks, and that q'_{t_m} grows further toward the peak. To attribute the source of this accumulation, we pose a budget for q_{t_m} along a trajectory and rewrite it into a budget for q'_{t_m} following Equation 7 (a similar budget for moist-static energy anomalies is included in Figure S6 in Supporting Information S1; it tells a qualitatively similar story as the analysis that follows):

$$\underbrace{\partial_t q'_{t_m} + u_{h_l}\partial_x q'_{t_m}}_{\text{Tendency}} = \underbrace{-w'_m \partial_z q_{t_l}}_{\text{Vertical advection}} \underbrace{-\frac{1}{\rho_0}\partial_z\left[\rho_0\left(\left(w'_s q'_{t_s}\right)_m - \left(w'_s q'_{t_s}\right)_l\right)\right]}_{\text{Vertical flux conv.}} + \underbrace{\frac{1}{\rho_0}\partial_z P'_m}_{\text{Precipitation}} + \underbrace{\mathcal{R}}_{\text{Residual (hor. trans.)}}, \tag{13}$$

In this relation, the divergence of warm precipitation fluxes is the only source, and we assume that the residual $\mathcal{R}$ mainly describes the horizontal transport out of a mesoscale column as it is translated along a trajectory with u_{h_l}. We plot the terms in this budget for Q1 trajectories relative to mean trajectories in Figures 8a–8e.

First, we observe that the main source for the growth of q'_{t_m} in Q1 blocks is the vertical advection with w'_m (Figure 8b). Given WTG and plugging Equation 8 into Equation 13, we can for the cloud layer express this term as

$$-w'_m \partial_z q_{t_l} \approx -\frac{\alpha}{\rho_0}\left(\partial_z\left(\rho_0 F_{\theta'_{lv_m}}\right) + \frac{1}{c_p \Pi}\partial_z\left(\mu L_v P'_m\right)\right) \tag{14}$$

where $\alpha = -\partial_z q_{t_l}/\partial_z \theta_{lv_l}$, an analogy of Chikira (2014)'s parameter, quantifies how efficiently a mesoscale heating perturbation translates to mesoscale moistening under WTG (Figure 8f). Because of the convex relationship between q_{t_l} and θ_{lv_l}, $\alpha > 0$ throughout the cloud layer, and grows especially large across the transition layer near cloud base (Albright et al., 2023; Bretherton & Blossey, 2017; Janssens et al., 2023); it is also almost constant across the moist anomalies' life cycle. Therefore, the anomalous turbulent heat flux convergence (Figure 8g), carried by condensational heating anomalies, place the peak of $-w'_m \partial_z q_{t_l}$ in the lower cloud layer, while the

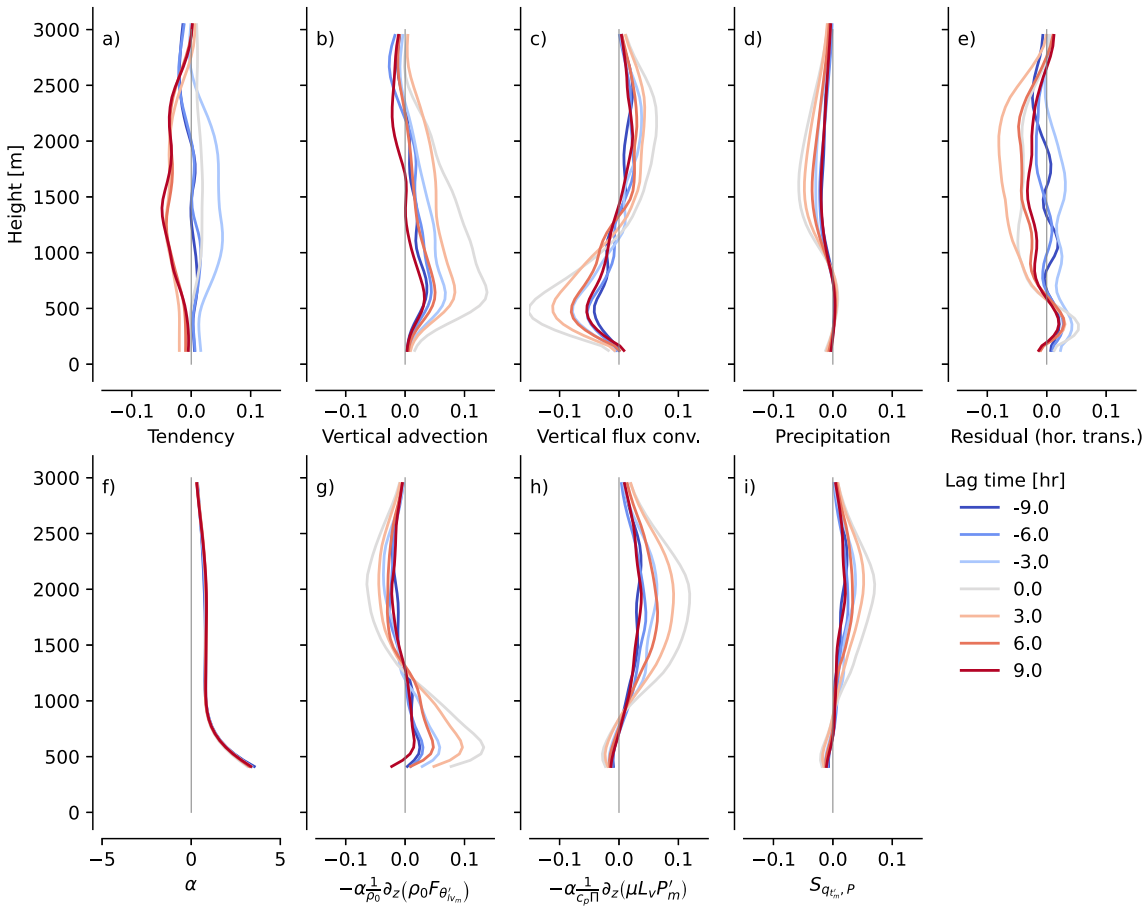

Figure 8. (a–e): Terms in the moisture budget Equation 13, for Q1 trajectories relative to the mean trajectory in the domain at a given launch time. The terms are then averaged over all launch times. (f) The Chikira parameter α; (g, h): Vertical moisture advection (b) decomposed into contributions from anomalous heat fluxes (g) and precipitation (h) according to Equation 14; (i) the total moisture source from precipitation (Equation 15). All units are g kg^{-1} hr^{-1}, except α (g kg^{-1} K^{-1}).

precipitation heating (Figure 8h) prevents drying in the lower free troposphere (1,500–3,000 m) from an anomalous heat flux divergence (Figure 8g), associated with evaporative cooling fluctuations.

Anomalously strong small-scale moisture fluxes then transport q'_{t_m} to the upper cloud layer (Figure 8c), where they partially rain out (Figure 8d). However, gathering the terms scaling $\partial_z P'_m$ in Equations 13 and 14 in a net precipitation moistening term

$$S_{q_{t_m},P} = \left(1 - \frac{\alpha \mu L_v}{c_p \Pi}\right) \frac{1}{\rho_0} \partial_z P_m, \tag{15}$$

reveals that the moistening contribution from the precipitation's heating always outweighs its direct drying (Figure 8i), that is, $S_{q_{t_m},P} > 0$ for the given α. In sum, while the vertical motions strengthen, the q'_{t_m} tendency (Figure 8a) is positive because horizontal export of q'_{t_m} from moist regions (Figure 8e) is too small to oppose the convectively driven moistening. That is, as in idealized LESs, vertical advection with mesoscale circulations aggregates q_{t_m} into more strongly convecting regions, and if the convective heating is indeed controlled by column moisture, they grow through a moisture-convection feedback. In contrast to idealized LESs, these moist anomalies are present in the large-scale flow already when it enters the ICON domain (Figure 7c), also emphasizing the importance of processes which set such anomalies outside the trades (e.g., Aemisegger et al., 2021; Villiger et al., 2022).

The unbounded growth of the moisture anomalies is prevented by a rise in the terms subsumed under $\mathcal{R}$ (Figure 8e) over the second half of the trajectories. These dry out the moist, convecting columns, which then

21698996, 2024, 18, Downloaded from https://agupubs.onlinelibrary.wiley.com/doi/10.1029/2024JD041417 by Technical University Delft, Wiley Online Library on [02/10/2024]. See the Terms and Conditions (https://onlinelibrary.wiley.com/terms-and-conditions) on Wiley Online Library for rules of use; OA articles are governed by the applicable Creative Commons License

21698996, 2024, 18, Downloaded from https://agupubs.onlinelibrary.wiley.com/doi/10.1029/2024JD041417 by Technical University Delft, Wiley Online Library on [02/10/2024]. See the Terms and Conditions (https://onlinelibrary.wiley.com/terms-and-conditions) on Wiley Online Library for rules of use; OA articles are governed by the applicable Creative Commons License

convect less strongly, ultimately reducing the heat sources and their vertical advective moistening (Figures 8b, 8g, and 8h). If $\mathcal{R}$ indeed predominantly expresses horizontal advection, as seems likely given its importance in earlier case studies, it reduces q'_{t_m} through small-scale mixing and through the diverging branches of mesoscale circulations (Janssens et al., 2023). Conversely, vertical shear in u_{h_l} (second term in Equation 13's tendency) can horizontally advect the upper-cloud layer moisture away, relative to the mean wind with which we trace the trajectories (Blossey et al., 2021), and large-scale subsidence can dampen them toward the surface (Bretherton & Blossey, 2017). To understand why and how fast mesoscale circulations decay, we must trace trajectories with a higher temporal frequency than done here, to estimate these individual processes accurately.

6. Summary and Outlook

Traditionally, the trades are viewed as areas where the large-scale tropical circulation descends, and this subsidence (w_l) controls shallow convection. However, recent studies (Bony & Stevens, 2019; George et al., 2023; Stephan & Mariaccia, 2021) find shallow vertical motion amplitudes over 100–400 km domains which are many times larger than what the traditional theory demands, requiring new theories for the coupling between shallow convection and circulations. Here, we have bridged the gap between the recent observations and theoretical ideas from idealized modeling studies (Bretherton & Blossey, 2017; Janssens et al., 2023). We confirm the consistent presence of 200 km-scale vertical motion amplitudes in satellite retrievals, in-situ observations and realistic LESs from the EUREC^{4}A field campaign (Figure 3). These shallow mesoscale vertical motions (w_m) blanket the lower atmosphere, are often organized in shallow circulations and develop without creating large, mesoscale buoyancy anomalies. That is, as envisioned by Bretherton and Blossey (2017), the simulated cloud-layer buoyancy budget satisfies a WTG balance (Figure 4), between scales of at least 12.5–400 km (Figure 6) across a month of realistic weather.

To explain the origins of w_m, we evaluate the buoyancy budget, which shows that w'_m balances mesoscale fluctuations in convective heating, partitioned between heat flux convergence and rain sedimentation. In ascending branches of shallow circulations, the ascent mostly takes place in active cumuli, as mass fluxes through larger cloud-base cloud fractions. Its compensating subsidence is exported from the ascending regions by gravity waves. Regions with less convection import this compensating subsidence, forming descending branches of circulations (Figure 5; a visual recapitulation is offered in Figure 1). Mesoscale circulations in the trades are thus composed of variability in condensation, rainfall, turbulence and waves, and are not directly driven by radiative cooling. Only at scales larger than roughly 700 km do the w_m amplitudes approach the measured and simulated campaign-average w_l associated with the wintertime climatology, and is the classical large-scale subsidence recovered.

Asking what controls w_m in the trades, is then equivalent to asking what controls the mesoscale patterning of shallow convective heating. The LES suggests that these patterns are not associated with variability in the surface buoyancy flux, but with cloud-layer moisture fluctuations (Figure 7), which are present in regions of mesoscale ascent up to 9 hr before the convection peaks, which amplify due to vertical transport with the ascent, and which decay with horizontal moisture export (Figure 8). In this view, the mesoscale vertical motion embodies the "reverberations" envisioned by Bony and Stevens (2019), between the moisture field, which sets the convection, and the convection, which sets the circulations that organize the moisture. Yet to fully unravel the role played by water vapor in this cloud-circulation coupling, we require more conclusive observations of the low-level humidity's covariability with near-surface divergence, and better theories for mesoscale water vapor-shallow convection interactions. More broadly, we lack a systematic synthesis of the many mechanisms that have in recent years been suggested to impact the mesoscale convective patterns in the trades. We hope such an assessment can emerge from analysis of Lagrangian trajectories—in long, large-domain LESs, in projects such as the forthcoming Lagrangian LES-MIP of EUREC^{4}A, and in satellite observations. Since all suggested mechanisms appear to pass through mesoscale circulations, WTG gives a useful frame for assembling the puzzle pieces from such studies.

Finally, our results emphasize that km-scale trade cumuli are not passive with respect to their larger-scale circulations. Averaged over mesoscale domains, shallow vertical motion is not an unambiguous CCF, nor a forcing that can simply be prescribed on idealized LES domains. Indeed, if the shallow clouds in the trades do respond to w_l, then the assumption is that the entire mesoscales, with all its circulations and associated cloud patterns, are controlled by such motion. Given the ability of the convection to self-invigorate and grow its scales, it is not

21698996, 2024, 18, Downloaded from https://agupubs.onlinelibrary.wiley.com/doi/10.1029/2024JD041417 by Technical University Delft, Wiley Online Library on [02/10/2024]. See the Terms and Conditions (https://onlinelibrary.wiley.com/terms-and-conditions) on Wiley Online Library for rules of use; OA articles are governed by the applicable Creative Commons License

obvious a priori how reasonable this assumption is. To conceptually understand what determines the cloudiness of the trades, we therefore require new theory, which consistently combines the classical ideas of shallow convective adjustment to large-scale forcing, with actively convecting mesoscales. The framework we sketch in Section 5, which naturally accommodates surface forcing and the effect of large-scale lapse rates, offers a promising starting point. Such theory could then inform both mesoscale LESs and climate model parameterizations of shallow convection, which must allow some exchange of the vertical motion generated by their simulated mass fluxes with adjacent mesoscale columns, if they wish to model the circulations they both currently miss (e.g., Jansson et al., 2023; Vogel et al., 2022). Promisingly, the data shows that ICON, at 312 m grid spacing, realistically represents the shallow mesoscale cloud-circulation coupling. Should the ongoing resolution revolution of climate modeling reach such grid spacings, we may begin to glimpse how clouds and circulations in the tropics are truly coupled.

Data Availability Statement

The EUREC^{4}A data used herein—from the ICON simulation (Schulz & Stevens, 2023), JOANNE (George, Stevens, Bony, Pincus, et al., 2021) and the sounding network (Stephan et al., 2020)—are openly available through the EUREC^{4}A intake catalog (EUREC4A community, 2023), see https://howto.eurec4a.eu/intro.html. The IASI CDR release we use is available from the EUMETSAT data store (EUMETSAT, 2022). C-2015 ASCAT data (Ricciardulli & Wentz, 2016) are produced by Remote Sensing Systems and sponsored by the NASA Ocean Vector Winds Science Team. Data are available at www.remss.com. The scripts used to post-process all data, and the data required to produce the figures in this paper, are available at https://doi.org/10.5281/zenodo.8095037 (Janssens, 2024).

Acknowledgments
MJ thanks Anna Lea Albright, Franziska Glassmeier, Jordi Vilà and Raphaela Vogel for insightful comments on an earlier version of this manuscript, and Thibaut Dauhut, Pier Siebesma, Chris Bretherton and Peter Blossey for subsequent discussions. We acknowledge Xuanyu Chen for suggesting to study the simulated surface forcing along Lagrangian trajectories, and Brandon Wolding and two anonymous reviewers for extensive and constructive reviews. MJ, GG and HS acknowledge support from the International Space Science Institute (ISSI) in Bern, through ISSI International Team project #576 ("Constraining Trade-Cumuli Feedback by Means of Process Understanding"). HS was funded by the Cooperative Institute for Climate, Ocean, & Ecosystem Studies (CICOES) under NOAA Cooperative Agreement NA20OAR4320271, Contribution No. 2024-1355. FC and DB were partly supported by CNES through the TOSCA PROCONUM project.

References

Acquistapace, C., Meroni, A. N., Labbri, G., Lange, D., Späth, F., Abbas, S., & Bellenger, H. (2022). Fast atmospheric response to a cold oceanic mesoscale patch in the north-western tropical Atlantic. *Journal of Geophysical Research: Atmospheres*, *127*(21), e2022JD036799. https://doi.org/10.1029/2022jd036799

Adames, Á. F. (2022). The basic equations under weak temperature gradient balance: Formulation, scaling, and types of convectively coupled motions. *Journal of the Atmospheric Sciences*, *79*(8), 2087–2108. https://doi.org/10.1175/jas-d-21-0215.1

Aemisegger, F., Vogel, R., Graf, P., Dahinden, F., Villiger, L., Jansen, F., et al. (2021). How Rossby wave breaking modulates the water cycle in the North Atlantic trade wind region. *Weather and Climate Dynamics*, *2*(1), 281–309. https://doi.org/10.5194/wcd-2-281-2021

Ahmed, F., Neelin, J. D., & Adames, Á. F. (2021). Quasi-equilibrium and weak temperature gradient balances in an equatorial beta-plane model. *Journal of the Atmospheric Sciences*, *78*(1), 209–227. https://doi.org/10.1175/jas-d-20-0184.1

Albrecht, B. A., Betts, A. K., Schubert, W. H., & Cox, S. K. (1979). Model of the thermodynamic structure of the trade-wind boundary layer: Part I. Theoretical formulation and sensitivity tests. *Journal of the Atmospheric Sciences*, *36*(1), 73–89. https://doi.org/10.1175/1520-0469(1979)036<0073:mottso>2.0.co;2

Albright, A. L., Bony, S., Stevens, B., & Vogel, R. (2022). Observed subcloud-layer moisture and heat budgets in the trades. *Journal of the Atmospheric Sciences*, *79*(9), 2363–2385. https://doi.org/10.1175/jas-d-21-0337.1

Albright, A. L., Stevens, B., Bony, S., & Vogel, R. (2023). A new conceptual picture of the trade-wind transition layer. *Journal of the Atmospheric Sciences*, *80*(6), 1547–1563. https://doi.org/10.1175/jas-d-22-0184.1

Alinaghi, P., Siebesma, P., Jansson, F., Janssens, M., & Glassmeier, F. (2024). External drivers and mesoscale self-organization of shallow cold pools in the trade-wind regime. *Authorea Preprints*. https://doi.org/10.22541/essoar.172097919.97430863/v1

Bellon, G., & Stevens, B. (2013). Time scales of the trade wind boundary layer adjustment. *Journal of the Atmospheric Sciences*, *70*(4), 1071–1083. https://doi.org/10.1175/jas-d-12-0219.1

Betts, A. K. (1973). Non-precipitating cumulus convection and its parameterization. *Quarterly Journal of the Royal Meteorological Society*, *99*(419), 178–196. https://doi.org/10.1256/smsqj.41913

Betts, A. K., & Ridgway, W. (1988). Coupling of the radiative, convective, and surface fluxes over the equatorial pacific. *Journal of the Atmospheric Sciences*, *45*(3), 522–536. https://doi.org/10.1175/1520-0469(1988)045<0522:cotrca>2.0.co;2

Betts, A. K., & Ridgway, W. (1989). Climatic equilibrium of the atmospheric convective boundary layer over a tropical ocean. *Journal of the Atmospheric Sciences*, *46*(17), 2621–2641. https://doi.org/10.1175/1520-0469(1989)046<2621:ceotac>2.0.co;2

Blossey, P. N., Bretherton, C. S., & Mohrmann, J. (2021). Simulating observed cloud transitions in the Northeast Pacific during cset. *Monthly Weather Review*, *149*(8), 2633–2658. https://doi.org/10.1175/mwr-d-20-0328.1

Blossey, P. N., Bretherton, C. S., Zhang, M., Cheng, A., Endo, S., Heus, T., et al. (2013). Marine low cloud sensitivity to an idealized climate change: The CGILS LES intercomparison. *Journal of Advances in Modeling Earth Systems*, *5*(2), 234–258. https://doi.org/10.1002/jame.20025

Bony, S., & Stevens, B. (2019). Measuring area-averaged vertical motions with dropsondes. *Journal of the Atmospheric Sciences*, *76*(3), 767–783. https://doi.org/10.1175/jas-d-18-0141.1

Bony, S., Stevens, B., Ament, F., Bigorre, S., Chazette, P., Crewell, S., et al. (2017). EUREC^{4}A: A field campaign to elucidate the couplings between clouds, convection and circulation. *Surveys in Geophysics*, *38*(6), 1529–1568. https://doi.org/10.1007/s10712-017-9428-0

Bretherton, C. S., & Blossey, P. N. (2017). Understanding mesoscale aggregation of shallow cumulus convection using large-eddy simulation. *Journal of Advances in Modeling Earth Systems*, *9*(8), 2798–2821. https://doi.org/10.1002/2017ms000981

Bretherton, C. S., & Park, S. (2008). A new bulk shallow-cumulus model and implications for penetrative entrainment feedback on updraft buoyancy. *Journal of the Atmospheric Sciences*, *65*(7), 2174–2193. https://doi.org/10.1175/2007jas2242.1

Bretherton, C. S., & Park, S. (2009). A new moist turbulence parameterization in the community atmosphere model. *Journal of Climate*, *22*(12), 3422–3448. https://doi.org/10.1175/2008jcli2556.1

Bretherton, C. S., & Smolarkiewicz, P. K. (1989). Gravity waves, compensating subsidence and detrainment around cumulus clouds. *Journal of the Atmospheric Sciences*, *46*(6), 740–759. https://doi.org/10.1175/1520-0469(1989)046<0740:gwcsad>2.0.co;2

Bretherton, C. S., & Wyant, M. C. (1997). Moisture transport, lower-tropospheric stability, and decoupling of cloud-topped boundary layers. *Journal of the Atmospheric Sciences*, *54*(1), 148–167. https://doi.org/10.1175/1520-0469(1997)054<0148:mtltsa>2.0.co;2

Chazette, P., Marnas, F., Totems, J., & Shang, X. (2014). Comparison of IASI water vapor retrieval with H_2O-Raman Lidar in the framework of the Mediterranean HyMeX and ChArMEx programs. *Atmospheric Chemistry and Physics*, *14*(18), 9583–9596. https://doi.org/10.5194/acp-14-9583-2014

Chen, X., Dias, J., Wolding, B., Pincus, R., DeMott, C., Wick, G., et al. (2023). Ubiquitous sea surface temperature anomalies increase spatial heterogeneity of trade wind cloudiness on daily time scale. *Journal of the Atmospheric Sciences*, *80*(12), 2969–2987. https://doi.org/10.1175/jas-d-23-0075.1

Chikira, M. (2014). Eastward-propagating intraseasonal oscillation represented by Chikira–Sugiyama cumulus parameterization. Part II: Understanding moisture variation under weak temperature gradient balance. *Journal of the Atmospheric Sciences*, *71*(2), 615–639. https://doi.org/10.1175/jas-d-13-038.1

Daleu, C. L., Plant, R. S., Woolnough, S. J., Sessions, S., Herman, M. J., Sobel, A., et al. (2015). Intercomparison of methods of coupling between convection and large-scale circulation: 1. Comparison over uniform surface conditions. *Journal of Advances in Modeling Earth Systems*, *7*(4), 1576–1601. https://doi.org/10.1002/2015ms000468

Dauhut, T., Couvreux, F., Bouniol, D., Beucher, F., Volkmer, L., Pörtge, V., et al. (2023). Flower trade-wind clouds are shallow mesoscale convective systems. *Quarterly Journal of the Royal Meteorological Society*, *149*(750), 325–347. https://doi.org/10.1002/qj.4409

Denby, L. (2020). Discovering the importance of mesoscale cloud organization through unsupervised classification. *Geophysical Research Letters*, *47*(1), e2019GL085190. https://doi.org/10.1029/2019gl085190

Dipankar, A., Stevens, B., Heinze, R., Moseley, C., Zängl, G., Giorgetta, M., & Brdar, S. (2015). Large eddy simulation using the general circulation model ICON. *Journal of Advances in Modeling Earth Systems*, *7*(3), 963–986. https://doi.org/10.1002/2015ms000431

Dixit, V., Nuijens, L., & Helfer, K. C. (2021). Counter-gradient momentum transport through subtropical shallow convection in ICON-LEM simulations. *Journal of Advances in Modeling Earth Systems*, *13*(6), e2020MS002352. https://doi.org/10.1029/2020ms002352

Eastman, R., Terai, C. R., Grosvenor, D. P., & Wood, R. (2021). Evaluating the Lagrangian evolution of subtropical low clouds in GCMS using observations: Mean evolution, time scales, and responses to predictors. *Journal of the Atmospheric Sciences*, *78*(2), 353–372. https://doi.org/10.1175/jas-d-20-0178.1

EUMETSAT. (2021). Validation report IASI level-2 T and q profiles (Tech. Rep. No. Release 1). In *European organisation for the exploitation of meteorological satellites*. https://doi.org/10.15770/EUM_SEC_CLM_0027

EUMETSAT. (2022). IASI all sky temperature and humidity profiles (Tech. Rep. No. Climate Data Record Release 1.1 - Metop-A and -B). In *European organisation for the exploitation of meteorological satellites*. https://doi.org/10.15770/EUM_SEC_CLM_0063

EUREC4A community. (2023). *EUREC^{4}A*. Zenodo. https://doi.org/10.5281/zenodo.8422322

Fildier, B., Muller, C., Pincus, R., & Fueglistaler, S. (2023). How moisture shapes low-level radiative cooling in subsidence regimes. *AGU Advances*, *4*(3). https://doi.org/10.1029/2023AV000880

George, G., Stevens, B., Bony, S., Klingebiel, M., & Vogel, R. (2021a). Observed impact of mesoscale vertical motion on cloudiness. *Journal of the Atmospheric Sciences*, *78*(8), 2413–2427. https://doi.org/10.1175/jas-d-20-0335.1

George, G., Stevens, B., Bony, S., Pincus, R., Fairall, C., Schulz, H., et al. (2021b). JOANNE: Joint dropsonde observations of the atmosphere in tropical north Atlantic Meso-scale environments. *Earth System Science Data*, *13*(11), 5253–5272. https://doi.org/10.5194/essd-13-5253-2021

George, G., Stevens, B., Bony, S., Vogel, R., & Naumann, A. K. (2023). Widespread shallow mesoscale circulations observed in the trades. *Nature Geoscience*, *16*(7), 584–589. https://doi.org/10.1038/s41561-023-01215-1

Golaz, J.-C., Larson, V. E., & Cotton, W. R. (2002). A PDF-based model for boundary layer clouds. Part I: Method and model description. *Journal of the Atmospheric Sciences*, *59*(24), 3540–3551. https://doi.org/10.1175/1520-0469(2002)059<3540:apbmfb>2.0.co;2

Held, I. M., & Hoskins, B. J. (1985). Large-scale eddies and the general circulation of the troposphere. *Advances in Geophysics*, *28*, 3–31. https://doi.org/10.1016/s0065-2687(08)60218-6

Hourdin, F., Jam, A., Rio, C., Couvreux, F., Sandu, I., Lefebvre, M.-P., & Idelkadi, A. (2019). Unified parameterization of convective boundary layer transport and clouds with the thermal plume model. *Journal of Advances in Modeling Earth Systems*, *11*(9), 2910–2933. https://doi.org/10.1029/2019ms001666

Janssens, M. (2023). *Mesoscale cloud patterns in the trade-wind boundary layer (Doctoral dissertation)*. Wageningen University and Research. https://doi.org/10.18174/635857

Janssens, M. (2024). Supporting data for Shallow convective heating in weak temperature gradient balance explains mesoscale vertical motions in the trades (previously for ch. 5 of mesoscale cloud patterns in the trade-wind boundary layer) [Dataset and software]. *Zenodo*. https://doi.org/10.5281/zenodo.10998663

Janssens, M., De Arellano, J. V.-G., Van Heerwaarden, C. C., De Roode, S. R., Siebesma, A. P., & Glassmeier, F. (2023). Nonprecipitating shallow cumulus convection is intrinsically unstable to length scale growth. *Journal of the Atmospheric Sciences*, *80*(3), 849–870. https://doi.org/10.1175/jas-d-22-0111.1

Janssens, M., Vilà-Guerau De Arellano, J., Scheffer, M., Antonissen, C., Siebesma, A. P., & Glassmeier, F. (2021). Cloud patterns in the trades have four interpretable dimensions. *Geophysical Research Letters*, *48*(5), e2020GL091001. https://doi.org/10.1029/2020gl091001

Jansson, F., Janssens, M., Grönqvist, J. H., Siebesma, P., Glassmeier, F., Attema, J. J., et al. (2023). Cloud botany: Shallow cumulus clouds in an ensemble of idealized large-domain large-eddy simulations of the trades. *Journal of Advances in Modeling Earth Systems*, *10*(11), e2023MS003796. https://doi.org/10.1029/2023ms003796

Klein, R. (2010). Scale-dependent models for atmospheric flows. *Annual Review of Fluid Mechanics*, *42*(1), 249–274. https://doi.org/10.1146/annurev-fluid-121108-145537

Klein, S. A., Hall, A., Norris, J. R., & Pincus, R. (2017). Low-cloud feedbacks from cloud-controlling factors: A review. In R. Pincus, M. Winker, S. Bony, & B. Stevens (Eds.), *Shallow clouds, water vapor, circulation, and climate sensitivity* (pp. 135–157). Springer.

Klingebiel, M., Konow, H., & Stevens, B. (2021). Measuring shallow convective mass flux profiles in the trade wind region. *Journal of the Atmospheric Sciences*, *78*(10), 3205–3214. https://doi.org/10.1175/jas-d-20-0347.1

Klinger, C., Mayer, B., Jakub, F., Zinner, T., Park, S.-B., & Gentine, P. (2017). Effects of 3-D thermal radiation on the development of a shallow cumulus cloud field. *Atmospheric Chemistry and Physics*, *17*(8), 5477–5500. https://doi.org/10.5194/acp-17-5477-2017

Konow, H., Ewald, F., George, G., Jacob, M., Klingebiel, M., Kölling, T., et al. (2021). EUREC^{4}A's HALO. *Earth System Science Data*, *13*(12), 5545–5563. https://doi.org/10.5194/essd-13-5545-2021

Kuang, Z. (2008). Modeling the interaction between cumulus convection and linear gravity waves using a limited-domain cloud system–resolving model. *Journal of the Atmospheric Sciences*, *65*(2), 576–591. https://doi.org/10.1175/2007jas2399.1

21698996, 2024, 18, Downloaded from https://agupubs.onlinelibrary.wiley.com/doi/10.1029/2024JD041417 by Technical University Delft, Wiley Online Library on [02/10/2024]. See the Terms and Conditions (https://onlinelibrary.wiley.com/terms-and-conditions) on Wiley Online Library for rules of use; OA articles are governed by the applicable Creative Commons License

Lamer, K., Kollias, P., & Nuijens, L. (2015). Observations of the variability of shallow trade wind cumulus cloudiness and mass flux. *Journal of Geophysical Research: Atmospheres*, *120*(12), 6161–6178. https://doi.org/10.1002/2014jd022950

Lewis, H., Bellon, G., & Dinh, T. (2023). Upstream large-scale control of subtropical low-cloud climatology. *Journal of Climate*, *36*(10), 3289–3303. https://doi.org/10.1175/jcli-d-22-0676.1

Lilly, D. K. (1968). Models of cloud-topped mixed layers under a strong inversion. *Quarterly Journal of the Royal Meteorological Society*, *94*(401), 292–309. https://doi.org/10.1002/qj.49709440106

Mapes, B. E. (1993). Gregarious tropical convection. *Journal of the Atmospheric Sciences*, *50*(13), 2026–2037. https://doi.org/10.1175/1520-0469(1993)050<2026:gtc>2.0.co;2

Menzel, W. P., Schmit, T. J., Zhang, P., & Li, J. (2018). Satellite-based atmospheric infrared sounder development and applications. *Bulletin of the American Meteorological Society*, *99*(3), 583–603. https://doi.org/10.1175/bams-d-16-0293.1

Muller, C. J., Yang, D., Craig, G., Cronin, T., Fildier, B., Haerter, J. O., et al. (2022). Spontaneous aggregation of convective storms. *Annual Review of Fluid Mechanics*, *54*(1), 133–157. https://doi.org/10.1146/annurev-fluid-022421-011319

Myers, T. A., & Norris, J. R. (2013). Observational evidence that enhanced subsidence reduces subtropical marine boundary layer cloudiness. *Journal of Climate*, *26*(19), 7507–7524. https://doi.org/10.1175/jcli-d-12-00736.1

Narenpitak, P., Kazil, J., Yamaguchi, T., Quinn, P. K., & Feingold, G. (2021). From sugar to flowers: A transition of shallow cumulus organization during ATOMIC. *Journal of Advances in Modeling Earth Systems*, *13*(10), e2021MS002619. https://doi.org/10.1029/2021ms002619

Naumann, A. K., Stevens, B., & Hohenegger, C. (2019). A moist conceptual model for the boundary layer structure and radiatively driven shallow circulations in the trades. *Journal of the Atmospheric Sciences*, *76*(5), 1289–1306. https://doi.org/10.1175/jas-d-18-0226.1

Naumann, A. K., Stevens, B., Hohenegger, C., & Mellado, J. P. (2017). A conceptual model of a shallow circulation induced by prescribed low-level radiative cooling. *Journal of the Atmospheric Sciences*, *74*(10), 3129–3144. https://doi.org/10.1175/jas-d-17-0030.1

Neggers, R. A. J., Stevens, B., & Neelin, J. D. (2006). A simple equilibrium model for shallow-cumulus-topped mixed layers. *Theoretical and Computational Fluid Dynamics*, *20*(5–6), 305–322. https://doi.org/10.1007/s00162-006-0030-1

Nicholls, M. E., Pielke, R. A., & Cotton, W. R. (1991). Thermally forced gravity waves in an atmosphere at rest. *Journal of the Atmospheric Sciences*, *48*(16), 1869–1884. https://doi.org/10.1175/1520-0469(1991)048<1869:tfgwia>2.0.co;2

Nuijens, L., Serikov, I., Hirsch, L., Lonitz, K., & Stevens, B. (2014). The distribution and variability of low-level cloud in the North Atlantic trades. *Quarterly Journal of the Royal Meteorological Society*, *140*(684), 2364–2374. https://doi.org/10.1002/qj.2307

Nuijens, L., Stevens, B., & Siebesma, A. P. (2009). The environment of precipitating shallow cumulus convection. *Journal of the Atmospheric Sciences*, *66*(7), 1962–1979. https://doi.org/10.1175/2008jas2841.1

Park, K.-A., Cornillon, P., & Codiga, D. L. (2006). Modification of surface winds near ocean fronts: Effects of gulf stream rings on scatterometer (QuikSCAT, NSCAT) wind observations. *Journal of Geophysical Research: Oceans*, *111*(C3). https://doi.org/10.1029/2005jc003016

Prange, M., Buehler, S. A., & Brath, M. (2023). How adequately are elevated moist layers represented in reanalysis and satellite observations? *Atmospheric Chemistry and Physics*, *23*(1), 725–741. https://doi.org/10.5194/acp-23-725-2023

Radtke, J., Naumann, A. K., Hagen, M., & Ament, F. (2022). The relationship between precipitation and its spatial pattern in the trades observed during EUREC^{4}A. *Quarterly Journal of the Royal Meteorological Society*, *148*(745), 1913–1928. https://doi.org/10.1002/qj.4284

Radtke, J., Vogel, R., Ament, F., & Naumann, A. K. (2023). *Spatial organisation affects the pathway to precipitation in simulated trade-wind convection*. Authorea. https://doi.org/10.22541/essoar.167979635.58663858/v1

Raymond, D. J., Fuchs, Ž., Gjorgjievska, S., & Sessions, S. (2015). Balanced dynamics and convection in the tropical troposphere. *Journal of Advances in Modeling Earth Systems*, *7*(3), 1093–1116. https://doi.org/10.1002/2015ms000467

Raymond, D. J., & Zeng, X. (2005). Modelling tropical atmospheric convection in the context of the weak temperature gradient approximation. *Quarterly Journal of the Royal Meteorological Society: A journal of the atmospheric sciences, applied meteorology and physical oceanography*, *131*(608), 1301–1320. https://doi.org/10.1256/qj.03.97

Ricciardulli, L., & Wentz, F. (2016). *ASCAT C-2015 daily ocean vector winds on 0.25 deg grid (Tech. Rep. No. Version 02.1 Daily)*. Remote Sensing Systems. Retrieved from www.remss.com

Romps, D. M. (2012a). Numerical tests of the weak pressure gradient approximation. *Journal of the Atmospheric Sciences*, *69*(9), 2846–2856. https://doi.org/10.1175/jas-d-11-0337.1

Romps, D. M. (2012b). Weak pressure gradient approximation and its analytical solutions. *Journal of the Atmospheric Sciences*, *69*(9), 2835–2845. https://doi.org/10.1175/JAS-D-11-0336.1

Saffin, L., Lock, A., Tomassini, L., Blyth, A., Böing, S., Denby, L., & Marsham, J. (2023). Kilometer-scale simulations of trade-wind cumulus capture processes of mesoscale organization. *Journal of Advances in Modeling Earth Systems*, *15*(3), e2022MS003295. https://doi.org/10.1029/2022ms003295

Sakradzija, M., & Klingebiel, M. (2020). Comparing ground-based observations and a large-eddy simulation of shallow cumuli by isolating the main controlling factors of the mass flux distribution. *Quarterly Journal of the Royal Meteorological Society*, *146*(726), 254–266. https://doi.org/10.1002/qj.3671

Schulz, H. (2022). C3ontext: A common consensus on convective organization during the EUREC^{4}A experiment. *Earth System Science Data*, *14*(3), 1233–1256. https://doi.org/10.5194/essd-14-1233-2022

Schulz, H., & Stevens, B. (2018). Observing the tropical atmosphere in moisture space. *Journal of the Atmospheric Sciences*, *75*(10), 3313–3330. https://doi.org/10.1175/jas-d-17-0375.1

Schulz, H., & Stevens, B. (2023). Evaluating large-domain, hecto-meter, large-eddy simulations of trade-wind clouds using EUREC^{4}A data. *Journal of Advances in Modeling Earth Systems*, *15*(10), e2023MS003648. https://doi.org/10.1029/2023ms003648

Scott, R. C., Myers, T. A., Norris, J. R., Zelinka, M. D., Klein, S. A., Sun, M., & Doelling, D. R. (2020). Observed sensitivity of low-cloud radiative effects to meteorological perturbations over the global oceans. *Journal of Climate*, *33*(18), 7717–7734. https://doi.org/10.1175/jcli-d-19-1028.1

Seifert, A., Heus, T., Pincus, R., & Stevens, B. (2015). Large-eddy simulation of the transient and near-equilibrium behavior of precipitating shallow convection. *Journal of Advances in Modeling Earth Systems*, *7*(4), 1918–1937. https://doi.org/10.1002/2015ms000489

Siebesma, A. P., Bretherton, C. S., Brown, A., Chlond, A., Cuxart, J., Duynkerke, P. G., et al. (2003). A large eddy simulation intercomparison study of shallow cumulus convection. *Journal of the Atmospheric Sciences*, *60*(10), 1201–1219. https://doi.org/10.1175/1520-0469(2003)60<1201:alesis>2.0.co;2

Sobel, A. H., & Bretherton, C. S. (2000). Modeling tropical precipitation in a single column. *Journal of Climate*, *13*(24), 4378–4392. https://doi.org/10.1175/1520-0442(2000)013<4378:mtpias>2.0.co;2

Sobel, A. H., Nilsson, J., & Polvani, L. M. (2001). The weak temperature gradient approximation and balanced tropical moisture waves. *Journal of the Atmospheric Sciences*, *58*(23), 3650–3665. https://doi.org/10.1175/1520-0469(2001)058<3650:twtgaa>2.0.co;2

21698996, 2024, 18, Downloaded from https://agupubs.onlinelibrary.wiley.com/doi/10.1029/2024JD041417 by Technical University Delft, Wiley Online Library on [02/10/2024]. See the Terms and Conditions (https://onlinelibrary.wiley.com/terms-and-conditions) on Wiley Online Library for rules of use; OA articles are governed by the applicable Creative Commons License

Stephan, C. C., & Mariaccia, A. (2021). The signature of the tropospheric gravity wave background in observed mesoscale motion. *Weather and Climate Dynamics*, *2*(2), 359–372. https://doi.org/10.5194/wcd-2-359-2021

Stephan, C. C., Schnitt, S., Schulz, H., Bellenger, H., De Szoeke, S. P., Acquistapace, C., & others (2020). Ship-and island-based atmospheric soundings from the 2020 EUREC4A field campaign. *Earth System Science Data Discussions*, *2020*, 1–35.

Stevens, B. (2006). Bulk boundary-layer concepts for simplified models of tropical dynamics. *Theoretical and Computational Fluid Dynamics*, *20*(5), 279–304. https://doi.org/10.1007/s00162-006-0032-z

Stevens, B. (2007). On the growth of layers of nonprecipitating cumulus convection. *Journal of the Atmospheric Sciences*, *64*(8), 2916–2931. https://doi.org/10.1175/jas3983.1

Stevens, B., Ackerman, A. S., Albrecht, B. A., Brown, A. R., Chlond, A., Cuxart, J., et al. (2001). Simulations of trade wind cumuli under a strong inversion. *Journal of the Atmospheric Sciences*, *58*(14), 1870–1891. https://doi.org/10.1175/1520-0469(2001)058<1870:sotwcu>2.0.co;2

Stevens, B., Bony, S., Brogniez, H., Hentgen, L., Hohenegger, C., Kiemle, C., et al. (2020). Sugar, gravel, fish and flowers: Mesoscale cloud patterns in the trade winds. *Quarterly Journal of the Royal Meteorological Society*, *146*(726), 141–152. https://doi.org/10.1002/qj.3662

Stevens, B., Bony, S., Farrell, D., Ament, F., Blyth, A., Fairall, C., & others (2021). EUREC4A. *Earth System Science Data*, *13*(8), 4067–4119.

Stevens, B., Brogniez, H., Kiemle, C., Lacour, J.-L., Crevoisier, C., & Kiliani, J. (2018). Structure and dynamical influence of water vapor in the lower tropical troposphere. In R. Pincus, M. Winker, S. Bony, & B. Stevens (Eds.), *Shallow clouds, water vapor, circulation, and climate sensitivity* (pp. 199–225). Springer.

Stevens, B., & Seifert, A. (2008). Understanding macrophysical outcomes of microphysical choices in simulations of shallow cumulus convection. *Journal of the Meteorological Society of Japan. Ser. II*, *86*, 143–162. https://doi.org/10.2151/jmsj.86a.143

Vial, J., Vogel, R., & Schulz, H. (2021). On the daily cycle of mesoscale cloud organization in the winter trades. *Quarterly Journal of the Royal Meteorological Society*, *147*(738), 2850–2873. https://doi.org/10.1002/qj.4103

Vilà-Guerau De Arellano, J., Van Heerwaarden, C., Van Stratum, B., & Van Den Dries, K. (2015). *Atmospheric boundary layer: Integrating air chemistry and land interactions*. Cambridge University Press.

Villiger, L., Wernli, H., Boettcher, M., Hagen, M., & Aemisegger, F. (2022). Lagrangian formation pathways of moist anomalies in the trade-wind region during the dry season: Two case studies from EUREC4A. *Weather and Climate Dynamics*, *3*(1), 59–88. https://doi.org/10.5194/wcd-3-59-2022

Vogel, R., Albright, A. L., Vial, J., George, G., Stevens, B., & Bony, S. (2022). Strong cloud–circulation coupling explains weak trade cumulus feedback. *Nature*, *612*(7941), 696–700. https://doi.org/10.1038/s41586-022-05364-y

Walters, D., Baran, A. J., Boutle, I., Brooks, M., Earnshaw, P., Edwards, J., et al. (2019). The met office unified model global atmosphere 7.0/7.1 and jules global land 7.0 configurations. *Geoscientific Model Development*, *12*(5), 1909–1963. https://doi.org/10.5194/gmd-12-1909-2019

Wolding, B. O., Maloney, E. D., & Branson, M. (2016). Vertically resolved weak temperature gradient analysis of the m Adden-Julian Oscillation in sp-cesm. *Journal of Advances in Modeling Earth Systems*, *8*(4), 1586–1619. https://doi.org/10.1002/2016ms000724

Wood, R., & Field, P. R. (2011). The distribution of cloud horizontal sizes. *Journal of Climate*, *24*(18), 4800–4816. https://doi.org/10.1175/2011jcli4056.1

21698996, 2024, 18, Downloaded from https://agupubs.onlinelibrary.wiley.com/doi/10.1029/2024JD041417 by Technical University Delft, Wiley Online Library on [02/10/2024]. See the Terms and Conditions (https://onlinelibrary.wiley.com/terms-and-conditions) on Wiley Online Library for rules of use; OA articles are governed by the applicable Creative Commons License